8-25-2016

Remote Vibration Estimation Using Displaced Phase Center Antenna SAR in a Strong Clutter Environment

Justin Campbell

Justin B. Campbell

Candidate

Electrical and Computer Engineering

Department

This thesis is approved, and it is acceptable in quality and form for publication:

Approved by the Thesis Committee:

Majeed Hayat , Chairperson

Admin Doerry

Walter Gerstle

Remote Vibration Estimation Using Displaced Phase Center Antenna SAR in a Strong Clutter Environment

by

Justin B. Campbell

B.S., Applied Mathematics, University of Arizona, 2011
B.F.A., Dance, University of Arizona, 2011

THESIS

Submitted in Partial Fulfillment of the
Requirements for the Degree of

Master of Science
Electrical Engineering

The University of New Mexico

Albuquerque, New Mexico

July, 2016

Dedication

To my parents, Steven and Susan, for their unrelenting support, and encouragement. This would not be possible without their backing. To my brother, Jesse, who has a work ethic second to none,.

"When you follow a star you know you will never reach that star; rather it will guide you to where you want to go. ... So it is with the world. It will only ever lead you back to yourself." – Jeanette Winterson

Acknowledgments

I would like to thank my adviser, Professor Majeed Hayat, for training and helping me to develop into a professional engineer. I would also like to thank Dr. Armin Doerry and Dr. Thomas Atwood for the continued support both inside and outside the classroom. Lastly, I would like to thank Professor Walter Gerstle for sharing his knowledge of structures and for being on my committee.

This work was performed at the University of New Mexico and partially supported by the United States Department of Energy (Award No. DE-NA0002494) and Sandia National Laboratories.

Remote Vibration Estimation Using Displaced Phase Center Antenna SAR in a Strong Clutter Environment

by

Justin B. Campbell

B.S., Applied Mathematics, University of Arizona, 2011
B.F.A., Dance, University of Arizona, 2011

M.S., Electrical Engineering, University of New Mexico, 2016

Abstract

Synthetic aperture radar (SAR) is a ubiquitous remote sensing platform that is used for numerous applications. In its most common configuration, SAR produces a high-resolution, two-dimensional image of a scene of interest. An underlying assumption when creating this high resolution image is that all targets in the ground scene are stationary throughout the duration of the image collection. If a target is not static, but instead vibrating, it introduces a modulation on the returned radar signal termed the micro-Doppler effect. The ability to estimate the target's vibration frequency and vibration amplitude by exploiting the micro-Doppler effect, all while in a high clutter environment can provide strategic information for target identification and target condition/status. This thesis discusses one method that processes the non-stationary signal of interest generated by the vibrating target in displaced phase center antenna (DPCA)-SAR in high clutter. The method is based on the extended Kalman filter (EKF) first proposed by Dr. Wang in his PhD dissertation titled *Time-frequency*

Methods for Vibration Estimation Using Synthetic Aperture Radar [24]. Previously, *EKF method* could accurately estimate the target's vibration frequency for single component sinusoidal vibrations. In addition, the target's vibration amplitude and position could be tracked throughout the duration of the aperture for single component sinusoidal vibrations. This thesis presents a modification to the *EKF method*, which improves the *EKF method's* overall performance. This modification improves the tracking capability of single component vibrations and provides reliable position tracking for several other different types of vibration dynamics. In addition, the *EKF method* is more reliable at higher noise levels. More specifically, for a single component vibration, the mean square error (MSE) of the original method is .2279, while the MSE of the method presented in this paper is .1503. Therefore, the method presented in this paper improves the position estimate of the vibrating target by 34% when SNR = 15 dB. For the multicomponent vibrations, the mean square error of the estimated target position is reduced by 76% when SNR = 15 dB. The original *EKF method* and the modified *EKF method* as well as simulations for various target vibration dynamics are provided in this thesis.

Contents

List of Figures

List of Figures

List of Tables

Glossary

ATI-SAR	along-track interferometric SAR
B	baseline–the distance between the fore and aft antenna
c	propagation velocity
$c(\tau)$	clutter signal
DFrFT	discrete fractional Fourier transform
DPCA-SAR	displaced phase center antenna–SAR
EKF	extended Kalman filter
f_c	carrier frequency
f_v	frequency of vibrating target
GMTI	ground moving target indicator
MDV	minimum detectable velocity
MMVF	maximum measurable vibration frequency
MMVV	maximum measurable vibration velocity
MSE	mean square error

Glossary

PFA	polar format algorithm
prf	pulse repetition frequency
pri or Δt	pulse repetition interval
RCS	radar cross section
SAR	synthetic aperture radar
SCR	signal to clutter ratio
SoI	signal of interest
SNR	signal to noise ratio
τ	slow time
u	distance to scene center in the azimuth direction
V_a	platform velocity
$w(\tau)$	noise signal

Chapter 1

Introduction

Synthetic aperture radar (SAR) is a ubiquitous coherent imaging radar that generates high resolution images. SAR operates by illuminating the target scene with electromagnetic radiation, typically in the microwave band, and measures the strength of the return signal. The final product is a two-dimensional image where each pixel in the image represents the reflectivity of a region with respect to the transmitted frequency [8]. Since SAR relies on active illumination, it can create high-resolution images in all-weather environments. Consequently, SAR imaging has some distinct advantages over optical images, as the quality of optical images is dependent on the current weather conditions and the time of day. This is because optical sensors are passive sensors where the region of interest is illuminated by an external source such as the sun or moon. The typical range of these systems can be anywhere from 25 km for the Lynx radar [21] to well over 800 km for the RADARSAT-2 [4]. These collection platforms can generate images at a variety of resolution scales. The Lynx radar has the ability to generate .1 m (4 in.) resolution images [21]. Figure 1.1a is an example of a 1 ft resolution SAR image [21]. Figure 1.1b is an optical image from Google Maps of the same geographical location. Please note these two images were not taken at the same time. Therefore, there are, assuredly, some differences in the

(a) 1 ft. SAR image of a railroad bridge near Belen, NM over the Rio Grande river. The image was taken with the Lynx radar [21].

(b) Optical image of a railroad bridge near Belen, NM over the Rio Grande river. The image is from Google Maps.

Figure 1.1: There is a clear difference between the prominent features in a SAR image and the prominent features in an optical image. For example, the train tracks are more eye-catching in the SAR image, while the dirt roads are more pronounced in the optical image.

water level of the river. Regardless, one can still observe clear differences between the prominent features in a SAR image and the prominent features in an optical image. For example, the train tracks are more eye-catching in the SAR image, while the dirt roads are more pronounced in the optical image.

While SAR is adept at creating high resolution images, it is not limited to this single application. SAR is also proficient at collecting coherent data for a variety of other applications such as creating digital elevation maps, tracking temporal changes in a region of interest (also known as coherent change detection), detecting moving targets, terrain motion mapping, or determining oceanic surface conditions, to name a few [10]. Lastly, to demonstrate SAR's prominence and versatility, a SAR system was placed on the Lunar Reconnaissance Orbiter to provide a detailed terrain map of the moon to help plan for a future lunar base [3].

1.1 SAR Vibrometry

For common imaging applications, a typical airborne SAR platform illuminates the ground scene for at least several seconds to create a single SAR image. During the data-collection process, the image formation algorithm, often polar format algorithm (PFA), assumes all targets in the ground scene are stationary. This assumption makes SAR particularly sensitive to low-level target vibrations [1,2,13,15–17,19,30]. More specifically, ground target vibrations introduce a phase modulation, termed the micro-Doppler effect [2], into each returned SAR signal. Any vibrating target, with a strong radar cross section (RCS) relative to its surroundings will produce observable artifacts in the image called ghost targets. These ghost targets degrade the image quality, as it is impossible to distinguish real objects from ghost targets. An example of these ghost target's is shown in Fig. 1.2. While ground target vibrations affect the quality of a SAR image [15], [2], the image can contain vital information about the target's vibration frequency and vibration amplitude, if reliably detected. In turn, this vibration history could possibly identify the target and determine its current state or operating condition. Therefore, it is beneficial to have the capability of remotely estimating target vibrations, especially when physical or direct access to these objects is not possible.

It is important to reemphasize that SAR's sensitivity to low level target vibrations infers that it already has the inherent capability for remote vibration estimation. However, SAR systems are typically not designed to enhance or improve this modality. Moreover, this modality is hardly ever used or exploited. This thesis outline's the system parameters and the processing algorithm that will optimize the utility of this vibrometry modality.

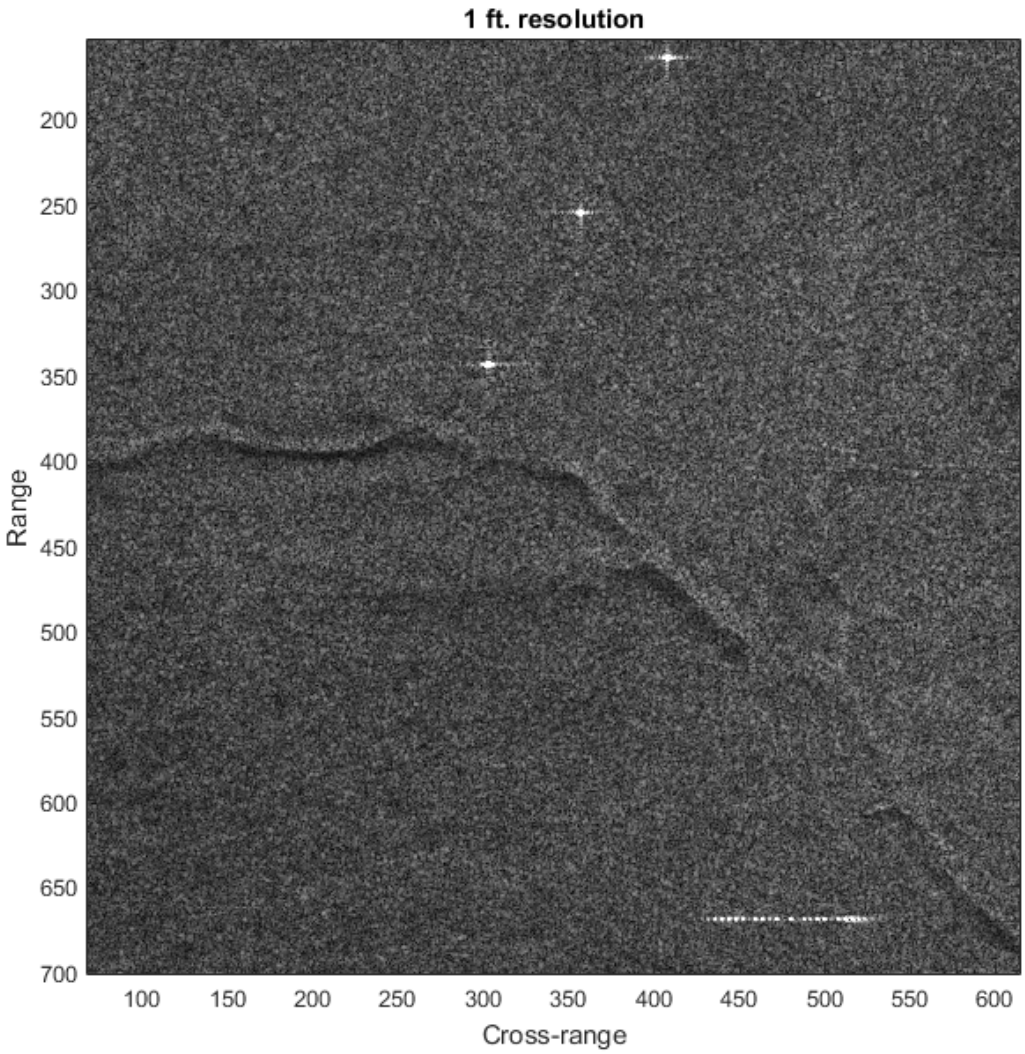

Figure 1.2: In the bottom right part of the image is a vibrating corner reflector with a lateral length of .53 m (21 in). This target had a vibration amplitude in the range direction of 1.5 cm (.59 in.) and a vibration frequency of 0.8 Hz. The ghost targets are spread in azimuth at the same range line. The other bright spots in the image are from static corner reflectors. The image was generated by the GA-ASI Lynx SAR system in collaboration with the University of New Mexico for various vibromtery experiments. The image has a .3 m (1 ft.) resolution.

1.2 Current SAR Vibrometry Methods

Previously, a remote vibration estimation technique that utilizes the Discrete Fractional Fourier Transform (DFrFT) on complex SAR images was introduced by the

Radar Vibrometry Group at the University of New Mexico. [25–28]. Using a complex image created through spotlight-mode SAR, the DFrFT method can accurately estimate a target's instantaneous acceleration, when the vibration of interest occurs in the range direction. This DFrFT method exploits the micro-Doppler effect that all vibrating targets engender onto the returned SAR signal. The micro-Doppler manifests itself as an instantaneous linear chirp in the slow-time signal. This technique is valuable as spotlight-mode SAR is utilized for a plethora of applications to create high-resolution 2-dimensional images. Incorporating radar vibrometry analysis on these images, the 2-dimensional complex SAR image becomes a 3-dimensional data set. The additional dimension contains the vibration information of each target in the ground scene, thus increasing the types of analysis performed on a single image. While the DFrFT is an effective remote vibration estimation tool, when the vibrating target is in a high clutter environment, signal to clutter ratio (SCR) $\leq$ 8 dB, the DFrFT does not always provide reliable results [29]. Therefore, an accurate remote vibration estimation in a high clutter environment is a necessity. The purpose of this thesis is to continue to refine and enhance an existing method for remote vibration estimation in a high clutter environment for numerous vibrating dynamics.

1.3 DPCA-SAR

Another ubiquitous remote sensing technique is the displaced phase center antenna for ground moving target applications (DPCA-GMTI). DPCA-GMTI is capable of characterizing and exploiting the Doppler shift caused by moving targets to determine the moving target's position and velocity, while in a high clutter environment. Although a typical SAR image collect lasts several seconds, DPCA-GMTI only lasts a small fraction of one second. Since the imaging time is significantly less for DPCA-GMTI, the resolution with be much finer than that of a SAR image. Therefore, to

have the Doppler resolution of SAR image with the robustness to clutter offered by the DPCA-GMTI, this thesis proposes performing DPCA-GMTI using SAR. The acronym DPCA-SAR, it used to represent this process. DPCA-SAR is a single-pass collection platform where, in effect, two SAR images, having only a temporal separation, are combined to provide a ground moving target indicator (GMTI) system. DPCA-SAR systems are robust in high clutter environments, a notable advantage over spotlight-mode SAR. Thus, DPCA-SAR is a particularly appealing platform for SAR vibrometry. However, while DPCA-SAR is robust in high clutter environments, the process of combining the two images to remove the static background (clutter) also removes the instantaneous linear chirp. Without this linear chirp in the slow-time signal, the DFrFT cannot be utilized for SAR vibrometry. Therefore, an alternative SAR vibrometry technique is required.

1.4 MDV and MMVF

As mentioned previously, DPCA is often used for GMTI applications. Therefore, this system is adept at processing Doppler signals generated from moving targets. A fundamental characterization of a GMTI system is its minimum detectable velocity (MDV). It is important to note that this minimum velocity is a minimum radial velocity difference between target and nominal clutter in the center of the antenna illumination, where the collection platform is viewed as the origin. Also, it is mandatory the target must be located inside the radar beam. A non-stationary target, which has total net velocity much greater than the MDV, but whose radial velocity is much smaller than MDV will not be reliably detected.

Since the collection platform is moving, all objects in the ground scene are going to create a Doppler shift on the incident signal. This Doppler shift is a function of range, azimuth, and the collection geometry. The collection of Doppler frequencies that has

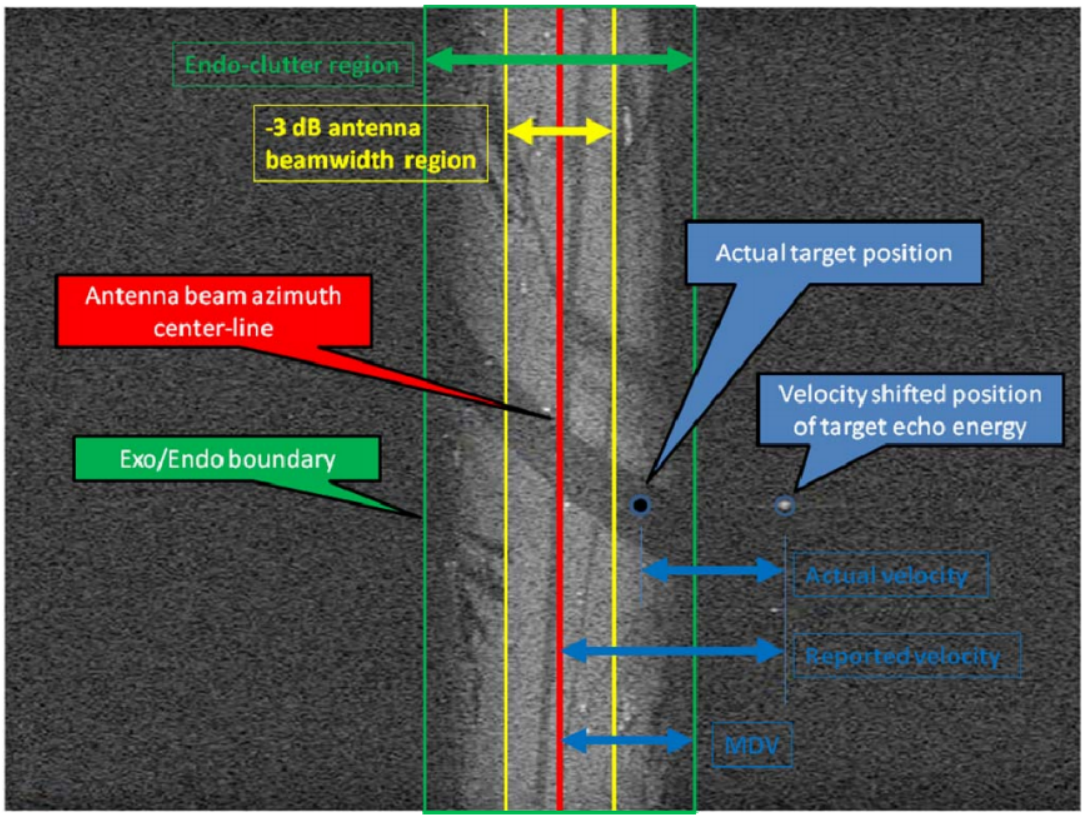

Figure 1.3: Range-Doppler map showing relationship between various GMTI parameters and measures. Data was collected at broadside geometry, [7].

significant energy from stationary targets is termed the endo-clutter region. The collection of Doppler frequencies that has negligible energy from stationary targets is termed the exo-clutter region [7]. If the moving target is moving faster than the MDV, then the moving target's reflected energy is shifted from the endo-clutter region and placed into the exo-clutter region. When the target's energy is placed in the exo-clutter region, its position and velocity can be more reliably determined. The endo-clutter region and the exo-clutter region can be visualized in Fig. 1.3. Fig. 1.3 is provided from [7], page 54.

For a single component, sinusoidal displacement, the maximum vibrational ve-

locity can be described as,

$$v_d = 2\pi f_v r_d, \tag{1.1}$$

where f_v is the vibration frequency, r_d is the vibration displacement, and v_d is the vibration velocity. Then, the minimum measurable vibration frequency (MMVF) is

$$f_v = \frac{v_d}{2\pi r_d}. \tag{1.2}$$

Note the single-beam, or single phase-center, Lynx radar system has a stated MDV of 5.8 kts or 2.984 m/s [21]. Then, set $v_d = 2.984$ m/s, and $r_d = .001$ m. Substituting these system parameters into (1.2), then MMVF is

$$\text{MMVF}_{GMTI} = 475\text{Hz}. \tag{1.3}$$

Any vibrating target with an amplitude of 1 mm and a vibration frequency less than 475 Hz, will have its energy centralized in the endo-clutter region. This makes it incredibly difficult to reliably determine any of its vibration characteristics. Therefore, in its single-channel GMTI applications, the Lynx radar system can only detect very high frequency vibrations, unless the target is significantly brighter than the surrounding clutter. Therefore, an alternative method for remote vibration estimation for lower frequencies is required.

References herein to the Lynx radar assume a single-beam, or single phase-center, mode of operation, as is customary for its SAR modes. While current versions of the Lynx radar offer multiple beams, allowing for clutter cancellation, these are conventionally used only in GMTI modes, and not for SAR modes. However, typically there is an increased Doppler frequency resolution in SAR modes over GMTI mode. Therefore, once again, combining the multiple beam characteristics of the GMTI mode while leveraging the Doppler frequency resolution in SAR is desired.

1.5 The Extended Kalman Filter Method

While low level vibrations cannot be reliably detected when in GMTI mode, DPCA-SAR's robustness in high clutter environments still makes it incredibly attractive for vibrometry applications. In this thesis, one method is revisited for remote vibrometry using DPCA-SAR. The method is based on the *extended Kalman filter* (EKF), which exploits both the magnitude and phase of the DPCA-SAR slow time signal. This method is used as a remote vibration estimation technique on DPCA-SAR platforms in high clutter environments.

In Dr. Qi Wang's PhD dissertation titled *Time-frequency Methods for Vibration Estimation Using Synthetic Aperture Radar* at the University of New Mexico in December 2012 [24], he initially proposed and discussed the *EKF method* for SAR vibrometry. For the *EKF method*, Dr. Wang introduced the method and gave examples of the method being applied to single component vibrations and multicomponent vibrations. The *EKF method* was very effective at determining the vibrating frequency and tracking the position of the vibrating target for single component vibrations. In addition, *EKF method* was sometimes able to estimate the frequencies of multicomponent vibrations. However, the *EKF method* did not always yield reliable results for estimating the target's position of multicomponent, linearly increasing, and linearly decreasing vibrations. Furthermore, the *EKF method* was susceptible to the state estimate diverging from the true state of the vibrating target.

1.6 Contributions of this Thesis

The emphasis of this thesis is refining and enhancing the *EKF method* first proposed by Dr. Wang [24]. This improvement is accomplished by introducing a state estimate averaging technique when linearizing the observation function. This modification

makes the *EKF method* more robust at lower SNR levels. This robustness decreases the likelihood of the state estimates diverging from the true state of the vibrating target. In some cases, the chances of a diverging solution is reduced by 60% (when SNR = 8 dB). In addition, the position of the vibrating target can be tracked more precisely. The enhanced *EKF method* is applied to sinusoidal vibrations, linearly increasing vibrations, linearly decreasing vibrations, and multicomponent vibrations. In each of the aforementioned vibration dynamics, the modified *EKF method* can track the position of the vibrating target and estimate the vibration frequency with greater accuracy than the original *EKF method*. For single component vibrations, the mean square error of the estimated target position is reduced by 34% when SNR = 15 dB. For the multicomponent vibrations, the mean square error of the estimated target position is reduced by 76% when SNR = 15 dB. The comparison to the modified *EKF method* presented in this thesis and the original *EKF method* proposed by Dr. Wang are displayed throughout the thesis. Lastly, the range of measurable vibration frequencies are characterized in terms of system parameters.

1.7 Organization of this Thesis

This thesis is organized as follows: the signal model for spotlight-mode SAR is defined and the signal model for DPCA-SAR is defined. In Dr. Wang's dissertation, he introduced a second vibrometry technique titled the *magnitude method* [24]. The *magnitude method* is reviewed here to provide motivation for the *EKF method* and the necessity of *EKF method's* improvement. With the necessary background established, the *EKF method* Dr. Wang developed is introduced. With Dr. Wang's method in hand, the modifications of *EKF method* are described and detailed. Finally, simulations and results of the modified *EKF method* are discussed.

Chapter 2

Signal Model

2.1 Signal model for spotlight-mode SAR

Throughout this thesis it is assumed the SAR collection system is operating in spotlightmode. In spotlight-mode SAR, the image is typically formed using the polar-format algorithm (PFA) [10]. In the PFA, the returned SAR signal is first demodulated and low-pass filtered. This is followed by a polar-to-rectangular re-sampling, which is applied to the SAR phase history to correct for irregular sample spacing due to the collection geometry. Next, an auto-focus method is usually applied to the reformatted SAR phase history to improve the quality of the SAR image [10]. Range compression is then applied to the SAR phase history to focus the targets on their correct range positions. The slow-time, τ, is defined as

$$\tau = u/V_a, \tag{2.1}$$

where u is the distance, in the azimuthal direction, from the antenna to the center of the ground scene and V_a is the speed of the SAR collection platform. The range-

compressed signal at a specified range can be written as

$$x(\tau) \approx \sum_i \overline{\sigma}_i \exp[jk_y y_i \tau - j\frac{4\pi}{\lambda} f_c r_i + j\phi_i] + \widetilde{w}(\tau), \tag{2.2}$$

where $\overline{\sigma}_i$ is the average reflectance of the ith target, y_i is the azimuthal position of the ith target, λ is the wavelength of the carrier frequency of the sent pulse, f_c is the carrier frequency of the sent pulse, r_i is range of the ith target, and ϕ_i is the initial phase of the ith target. The scalar, k_y, is a scaling parameter

$$k_y \approx \frac{4\pi f_c V_a}{cR_0 f_{prf}}, \tag{2.3}$$

where c is the propagation speed of the sent pulse, R_0 is the distance from the scene center to the mid-aperture, and f_{prf} is the pulse-repetition frequency (PRF). The additive noise $\widetilde{w}(\tau)$ is modeled as white zero-mean circularly-symmetric complex Gaussian (ZMCSCG) noise.

The range-compressed slow-time signal defined in (2.2) is valid only for static targets. When a vibrating target is present, y_i and r_i are no longer fixed and are functions of τ. Typically for an airborne system, R_0 is tens of kilometers making k_y much smaller than $4\pi f_c/c$. Thus, the phase modulation caused by changes in y_i are negligible and are, therefore, ignored. For completeness, $\overline{y}_i$ will denote the average cross-range position of the vibrating scatterer. By the same tack, small changes in r_i cause large fluctuations to the Doppler frequency, $f_y y_i$. This vibration-induced phase modulation is termed the micro-Doppler effect. The range compressed signal for a vibrating target is written as,

$$x(\tau) = \overline{\sigma}_v \exp[-jk_y \overline{y}_v \tau - j\frac{4\pi}{\lambda} x_v(\tau) + j\phi_v], \tag{2.4}$$

where $\overline{\sigma}_v$ is the average reflectance of the vibrating target, $\overline{y}_v$ is the average azimuthal position of the vibrating target, $x_v(\tau)$ is the position of the vibrating target in the range direction, and ϕ_v is the initial phase of the vibrating target.

The range-compressed signal with the vibrating target and the collection of static targets is defined as the SAR signal of interest (SoI), is written as [19], [2], [27]

$$\begin{aligned}\widetilde{s}(\tau) &= \widetilde{d}(\tau) + \widetilde{c}(\tau) + \widetilde{w}(\tau) \\ &\approx \overline{\sigma}_v \exp[-jk_y\overline{y}_v\tau - j\frac{4\pi}{\lambda}x_v(\tau) + j\phi_v] + \widetilde{c}(\tau) + \widetilde{w}(\tau)\end{aligned} \tag{2.5}$$

Signals from static targets on the ground are represented collectively by $\widetilde{c}(\tau)$. Conventionally $\widetilde{c}(\tau)$ is referred to as the clutter signal or simply clutter.

2.2 Signal Model for Displaced Phase Center-Synthetic Aperture Radar

Fig. 2.1 shows the data-collection geometry of the DPCA-SAR operating in ping-pong mode [31]. The baseline, B, is defined as the along-track spacing between the fore-antenna and the aft-antenna on the collection platform. In ping-pong mode, the fore-antenna collects data at a given location u^*, while the aft-antenna is off. Then the aft-antenna collects at the same location, u^*, with a time delay $\tau_B = B/V_a$, while the fore-antenna is off. This process repeats for the duration of the entire synthetic aperture. In this model, clutter is defined as any static target illuminated in the ground scene. For a particular range line, the slow-time clutter signal collected by the fore-antenna can be written as

$$c_1(\tau) = \sum_i \overline{\sigma}_i \exp[-jk_y y_i\tau - j\frac{4\pi}{\lambda}f_c r_i + j\phi_i]. \tag{2.6}$$

Since the clutter is static and the aft-antenna is illuminating the ground scene from the same location as the fore-antenna, the clutter will remain constant at every collection point u^* throughout the entire synthetic aperture. Therefore, for the same given range line, the slow-time clutter signal collected by the aft-antenna is the same

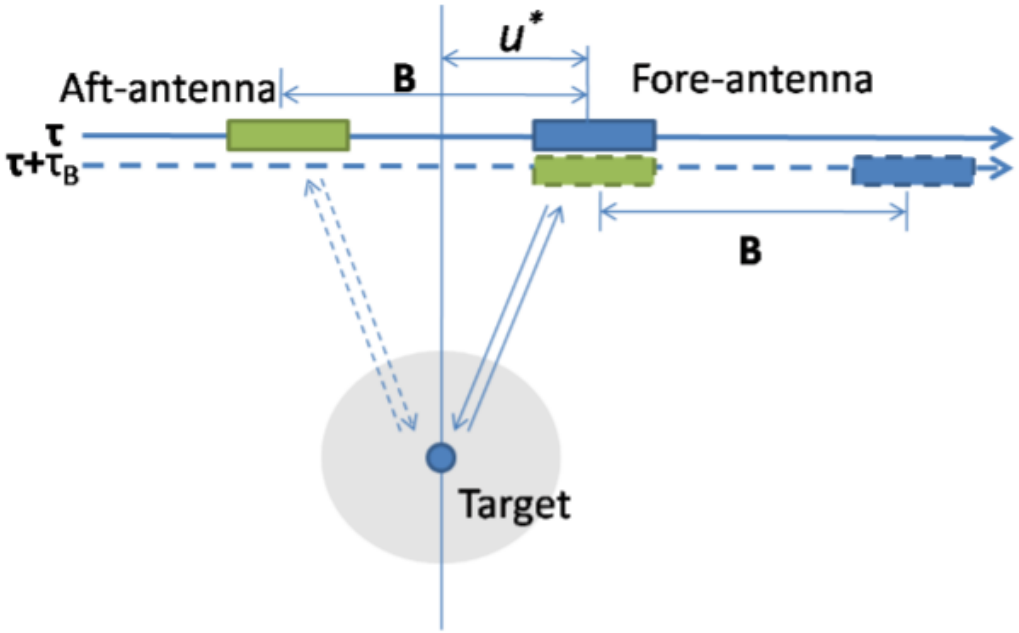

Figure 2.1: Data-collection geometry of the DPCA-SAR operating in ping-pong mode. The baseline, B, is defined as the distance between the fore-antenna and the aft-antenna. The aft-antenna collects the data from the same points as the fore-antenna with a time delay of $\tau_B = B/V_a$

clutter signal collected by the fore-antenna with a known time delay, τ_B,

$$\begin{aligned} c_2(\tau) &= c_1(\tau - \tau_B) \\ &= \sum_i \overline{\sigma}_i \exp[-jk_y y_i(\tau - \tau_B) - j\frac{4\pi}{\lambda} f_c r_i + j\phi_i], \end{aligned} \tag{2.7}$$

or equivalently,

$$\begin{aligned} c_2(\tau + \tau_B) &= c_1(\tau) \\ &= \sum_i \overline{\sigma}_i \exp[-jk_y y_i(\tau) - j\frac{4\pi}{\lambda} f_c r_i + j\phi_i]. \end{aligned} \tag{2.8}$$

Now consider a single vibrating target at a given range line. From the definition of the SAR SoI (2.5), the slow-time signal from a vibrating target collected by the

fore-antenna is

$$d_1(\tau) = \overline{\sigma}_v \exp[-jk_y\overline{y}_v\tau - j\frac{4\pi}{\lambda}x_v(\tau) + j\phi_v]. \tag{2.9}$$

Consequently, we can write the slow-time signal from the vibrating target collected by the aft-antenna, $d_2(\tau)$, as

$$d_2(\tau) = \overline{\sigma}_v \exp[-jk_y\overline{y}_v(\tau - \tau_B) - j\frac{4\pi}{\lambda}x_v(\tau) + j\phi_v]. \tag{2.10}$$

The first phase term of $d_2(\tau)$ is $-jk_y\overline{y}_v(\tau - \tau_B)$ as shown in the case of clutter. However, the second phase term of $d_2(\tau)$ remains the same as that for $d_1(\tau)$ because the aft-antenna also observes the instantaneous vibration displacement $x_v(\tau)$ at time τ. Equivalently, we have

$$d_2(\tau + \tau_B) = \overline{\sigma}_v \exp[-jk_y\overline{y}_v(\tau) - j\frac{4\pi}{\lambda}x_v(\tau + \tau_B) + j\phi_v]. \tag{2.11}$$

In summary, the two slow-time signals collected by the fore-antenna and the aft-antenna, from a ground scene containing a single vibrating target in clutter, can be written as

$$s_1(\tau) = d_1(\tau) + c_1(\tau) + w_1(\tau) \tag{2.12}$$

and

$$s_2(\tau) = d_2(\tau) + c_2(\tau) + w_2(\tau), \tag{2.13}$$

where d_1 and d_2 represent the signal from the vibrating target, c_1 and c_2 represent the clutter signal, and w_1 and w_2 represent the additive noise due to electronic error and quantization error, etc. Just as in the spotlight mode SoI, w_1 and w_2 are modeled as ZMCSCG noise.

Recall the clutter signal collected by the fore-antenna is the same as the clutter signal collected by the aft-antenna separated by a time delay, τ_B (2.7). By taking the

difference of the signals collected by the two antennas at the same collection location u^*, the clutter signal is totally removed and we obtain a signal that is modulated by the vibration dynamics in a non-linear manner. The difference signal $s(\tau)$, which is the DPCA SoI, is given by

$$\begin{aligned} s(\tau) &= s_2(\tau + \tau_B) - s_1(\tau) \\ &= d_2(\tau + \tau_B) + c_2(\tau + \tau_B) + w_2(\tau + \tau_B) - \\ &\qquad \big(d_1(\tau) + c_1(\tau) + w_1(\tau)\big) \\ &= d_2(\tau + \tau_B) - d_1(\tau) + w_2(\tau + \tau_B) - w_1(\tau). \end{aligned} \tag{2.14}$$

The operation represented by (2.14) is the DPCA technique [5]. In real-world applications, the removal of the clutter signal is subject to the noise floor of the DPCA-SAR system [5]. If we define

$$d(\tau) = d_2(\tau + \tau_B) - d_1(\tau) \tag{2.15}$$

and

$$w(\tau) = w_2(\tau + \tau_B) - w_1(\tau), \tag{2.16}$$

the DPCA-SAR SoI can be recast succinctly as

$$s(\tau) = d(\tau) + w(\tau). \tag{2.17}$$

2.3 Displaced Phase Center Antenna Synthetic Aperture Radar Signal of Interest

For a typical DPCA-SAR collection platform, τ_B is no more than a few milliseconds. If τ_B is much shorter than the duration of the vibration of interest, then the instantaneous vibration displacement approximation is

$$x_v(\tau + \tau_B) \approx x_v(\tau) + V_v(\tau)\tau_B, \tag{2.18}$$

where $V_v(\tau)$ is the instantaneous vibration velocity. With this assumption, $d(\tau)$ can be expressed, after some manipulations, as

$$d(\tau) \approx 2\sigma_v(\tau)\sin\left(\frac{2\pi\tau_B V_v(\tau)}{\lambda}\right)\times \exp\left[-j\frac{2\pi}{\lambda}(2x_v(\tau)+\tau_B V_v(\tau))-j\frac{\pi}{2}\right], \tag{2.19}$$

where

$$\sigma_v(\tau) = \overline{\sigma}_v \exp[-jk_y y_v \tau + j\phi_v]. \tag{2.20}$$

The complex-valued target reflectance $\sigma_v(\tau)$ can be estimated from the complex-valued SAR image [6, 10, 18]. The slow-time signal, $s(\tau)$, collected by the SAR platform is automatically sampled with the PRF. Therefore, the observed DPCA-SAR SoI can be written in discrete time as

$$s[n] = d[n] + w[n],\ n = 1, \ldots, N, \tag{2.21}$$

and

$$\sigma_v[n] = \overline{\sigma}_v \exp[-jk_y y_v n + j\phi_v], \tag{2.22}$$

where

$$d[n] = 2\sigma_v[n]\sin\left(\frac{2\pi\tau_B V_v[n]}{\lambda}\right)\times \exp\left[-j\frac{2\pi}{\lambda}(2x_v[n]+\tau_B V_v[n])-j\frac{\pi}{2}\right], \tag{2.23}$$

and N is the total number of the observed signal samples. The sampling interval, Δt, is the pulse-repetition interval (PRI) of the SAR system. The SNR of the DPCA-SAR SoI is defined as

$$\text{SNR} = 10\log_{10}\left(\frac{\overline{\sigma}_v^2}{\sigma_w^2}\right), \tag{2.24}$$

where σ_w^2 is the variance of $w[n]$. Equations (2.21)-(2.24) will be used in the observation model for the problem of vibration estimation using the DPCA-SAR platform.

There are two major differences between the DPCA-SAR SoI shown in (2.21) and the SAR SoI shown in (2.5) (also see (9) in [27]). First, both the magnitude and phase of $d[n]$ in the DPCA-SAR SoI are non-linearly modulated by the vibration dynamics. However, only the phase of $\tilde{d}[n]$ in the SAR SoI is linearly modulated by the vibration displacements. The DFrFT-based method is applicable when the magnitude of $\tilde{d}[n]$ remains the same (or changes very slowly compared to the vibration) [27], [29], and [22]. This is not the case for the DPCA-SAR SoI because the magnitude of $d[n]$ in the DPCA-SAR SoI changes as fast as the vibration velocity. Therefore, the DFrFT-based method is generally not applicable to the DPCA-SAR SoI. Second, the clutter signal is removed entirely from the DPCA-SAR SoI, while the SAR SoI suffers from the clutter signal. Because the DPCA-SAR SoI is only corrupted by additive noise as the clutter signal is removed, one can apply general signal estimation methods to the DPCA-SAR SoI for extracting $x_v[n]$ and $V_v[n]$. In this thesis, these vibration dynamics are estimated from the DPCA-SAR SoI using a method based on the extended Kalman filter (EKF). To achieve this, the *EKF method* will exploit information contained in both the envelope and the phase of the DPCA-SAR SoI.

Chapter 3

Magnitude Method

This chapter begins by reviewing the magnitude method first introduced by Dr. Wang [24]. Recall, both the magnitude and phase of $d[n]$ in the DPCA-SAR SoI are non-linearly modulated by the vibration dynamics of a vibrating target. Consider, for a moment, only the non-linearly modulated magnitude and disregard the phase. Then, the magnitude of $d[n]$ can be written as

$$|d[n]| = 2\overline{\sigma}_v \left| \sin\left(\frac{2\pi\tau_B}{\lambda} V_v[n] \right) \right|. \tag{3.1}$$

The instantaneous velocity $V_v[n]$ of a single-component sinusoidal vibration is

$$V_v[n] = M_v \cos(2\pi f_v \Delta t n + \psi_v) \tag{3.2}$$

where M_v is the magnitude of the velocity, f_v is the frequency of the vibration, Δt is the PRI, and ψ_v is the initial phase of the vibrating target. It is assumed that

$$M_v \leq \frac{\lambda}{4\tau_B}, \tag{3.3}$$

or equivalently

$$-\frac{\pi}{2} \leq \frac{2\pi\tau_B}{\lambda} V_v[n] \leq \frac{\pi}{2}. \tag{3.4}$$

When this assumption holds, there is a one-to-one correspondence between $V_v[n]$ and $|d[n]|$ when $V_v[n] > 0$ and there is the same one-to-one correspondence between $-V_v[n]$ and $|d[n]|$ when $V_v[n] \leq 0$. Therefore, the vibration behavior dictates that $|d[n]|$ repeats itself twice as fast as $V_v[n]$. Consequently, $|s[n]|$ also repeats itself twice as fast as $V_v[n]$, neglecting any interference from the additive noise. Provided that the SNR is sufficiently high, f_v can be estimated as half the frequency of $|s[n]|$. Because this method only requires the magnitude of the DPCA-SAR, we define it as the *magnitude method*.

The magnitude of the velocity of low-level vibration is usually quite small. For instance, the magnitude of the velocity of a 1 mm, 10 Hz vibration is approximately 0.0628 m/s. On the other hand, the maximum measurable vibration velocity (MMVV) is, $\lambda/4\tau_B$. For the Lynx radar system, this is approximately 0.2888 m/s. The maximum measurable vibration frequency (MMVF) is

$$MMVF = \frac{\lambda}{4\tau_B}\frac{1}{2\pi r_d}, \tag{3.5}$$

where r_d is the vibration displacement. For the Lynx radar system this is approximately 45 Hz. Therefore, the constraint in (3.4) can be satisfied for low-level vibrations of interest. Whenever $M_v > \lambda/\tau_B$, the mapping from $V_v[n]$ to $|d[n]|$, for either $V_v[n] > 0$ or $V_v[n] \leq 0$, is no longer bijective. In addition, harmonic frequencies of f_v appear in the spectrum of $|d[n]|$ that cause ambiguity in the estimated frequency.

3.1 Magnitude Method Simulations and Results

The proposed *magnitude method* in this thesis is validated by simulating the DPCA-SAR SoI (the returned observed SAR difference signal) in MATLAB. The simulated DPCA-SAR system is operating in the K_u-band. All of the key system parameters are listed in Table 6.1. These system parameters are chosen in part to mimic the

Table 3.1: Performance Limits of the *magnitude method* DPCA-SAR Vibration Estimation

parameter	quantity
Required SNR	4 dB
Frequency Resolution	$\frac{1}{f_{prf}N}$
MMVV	$\frac{\lambda}{4\tau_B}$
MMVF	$\frac{\lambda}{4\tau_B}\frac{1}{2\pi r_d}$

Lynx radar [21]. The baseline, B and the platform velocity, V_a are, however, notional values of a DPCA-SAR system. The DPCA-SAR SoI was generated using the model defined in (2.21) and (2.23).

Table 3.2: DPCA-SAR System Parameters Used In Simulations

parameter	quantity
center frequency	16 GHz
effective PRF	487 Hz
propagation velocity	3×10^8 m/s
platform velocity	175 m/s
slant range	10 km
azimuth resolution	.33 m
aperture length	363 m
SNR	11 dB
Baseline	0.3596 m

3.2 Sinusoidal vibration simulation

For the first set of simulations, consider a vibrating target whose displacement is described through a sinusoidal vibration with a constant frequency. The target had a 8 Hz oscillation with an amplitude of 1 mm. Fig. 3.1 shows the simulated DPCA-SAR signal. From the DPCA-SAR SoI, the target velocity is estimated using (3.1).

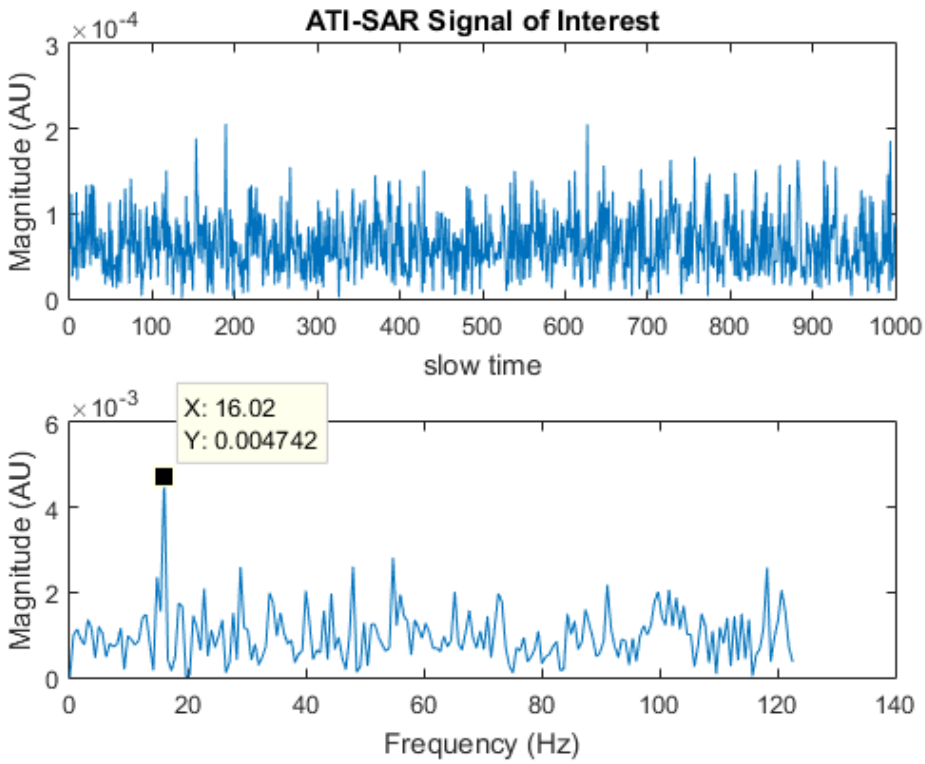

Figure 3.1: The top subplot is the magnitude of the DPCA-SAR SoI. The DPCA-SAR SoI was corrupted with ZMCSCG noise with a SNR of 4 dB. The bottom subplot is the power spectrum of the DPCA-SAR SoI. There is a distinct peak at 16.02 Hz. Since the SoI oscillates twice as fast as the vibrating target, the estimated vibration frequency is 8.01 Hz. Recall, the true target vibration is 8 Hz.

Fig. 3.2 shows the estimated target velocity. While the *magnitude method* estimates the vibration frequency quite well, it has difficulty estimating the target velocity accurately.

In an attempt to improve the estimated target velocity, the estimated velocity from the *magnitude method* is sent through a low pass filter. In particular, a 6 order Cheby2 with a stopband attenuation of 10 dB and a stopband edge frequency of 50 Hz was used from the MATLAB library. While Cheby2 filtered out the high frequency content, the estimated velocity is still unreliable. Fig. 3.3 shows the filtered velocity

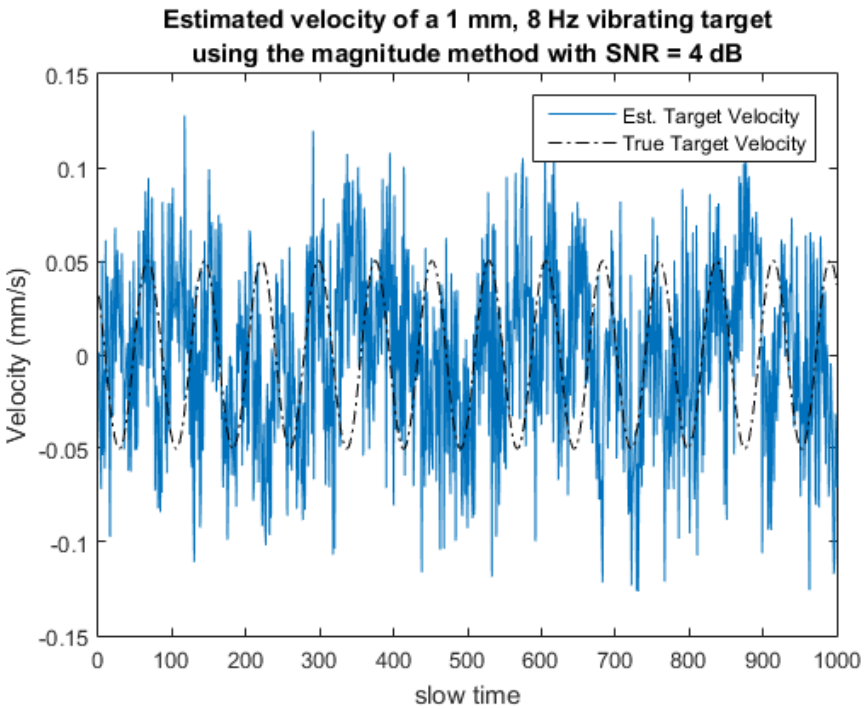

Figure 3.2: The estimated target velocity and the true target velocity are shown.

signal. The velocity estimate does not improve as the SNR increases.

Fig. 3.4 shows how the *magnitude method* performs under various SNR levels. The SNR is defined as

$$SNR = 10 \log_{10} \left(\frac{\sigma}{\sigma_w} \right), \tag{3.6}$$

where σ_w^2 is variance of the noise. With the target dynamics described above, 1,000 simulated slow-time DPCA-SAR SoIs were generated. Each realization of the slow-time signal was corrupted with ZMCSCG noise. Then, the aforementioned *magnitude method* was applied to each slow-time signal. If *magnitude method* reliably estimated the frequency of the vibrating target within 0.5 Hz, the estimation was considered to have converged. Otherwise, the method was considered to have diverged.

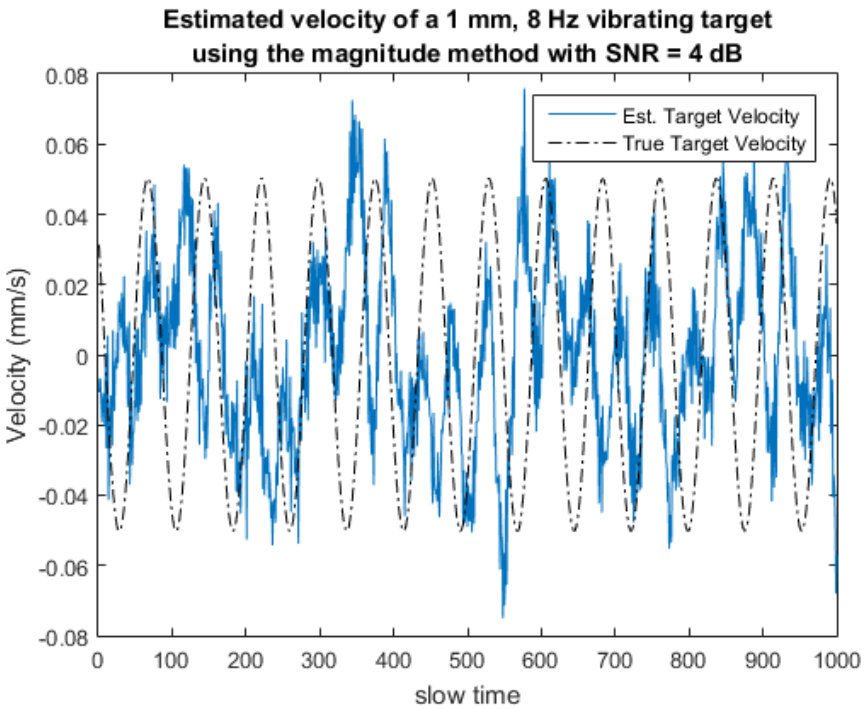

Figure 3.3: The estimated target velocity and the true target velocity are shown after applying a low pass filter.

3.3 Multicomponent vibration

The *magnitude method* is, in general, not applicable to multi-component vibrations. For instance, we can write $|d[n]|$ for a two component sinusoidal vibration as

$$\Big|d[n]\Big| = 2\overline{\sigma}_v \Big|\sin(k_1 v_1[n] + k_2 v_2[n])\Big|, \tag{3.7}$$

or equivalently,

$$\Big|d[n]\Big| = 2\overline{\sigma}_v \Big|\sin(k_1 v_1[n])\cos(k_2 v_2[n]) + \cos(k_1 v_1[n])\sin(k_2 v_2[n])\Big|, \tag{3.8}$$

where k_1 and k_2 are known scalars and $v_1[n]$ and $v_2[n]$ are the instantaneous velocities of the two vibrating components. The relation between the frequencies of $v_1[n]$ and $v_1[n]$ to the frequencies of $|d[n]|$ is not trivial. Thus, the *magnitude method* only works for fixed sinusoidal vibrations.

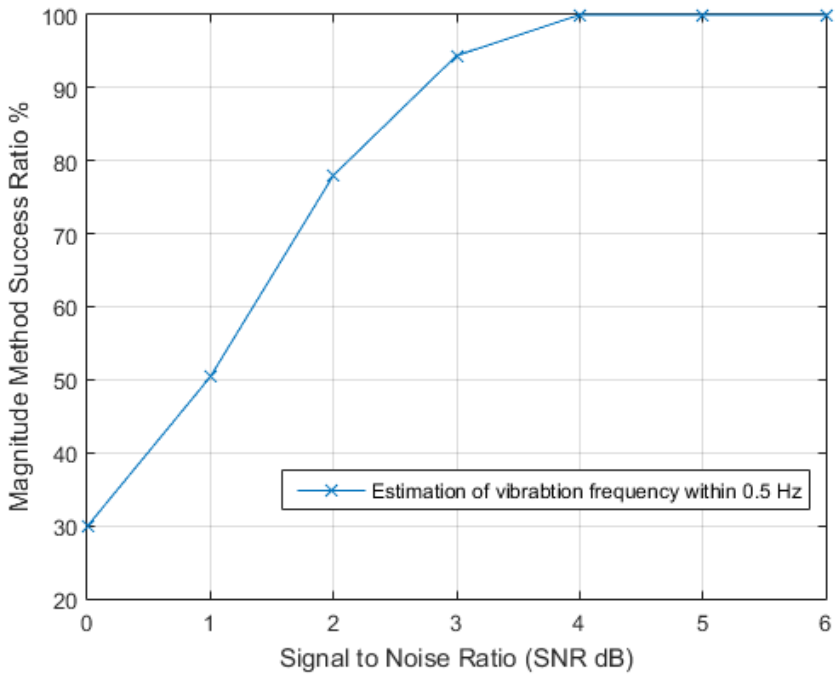

Figure 3.4: Success percentage of reliably estimating the frequency of the vibrating target within 0.5 Hz over 1,000 SoI for a given SNR. The vibrating target had a frequency of 8 Hz and a magnitude of 1 mm.

3.4 Summary

When considering a single component, sinusoidal vibration, the *magnitude method* can successfully estimate the frequency of a vibrating target as sufficient SNR levels. However, the *magnitude method* cannot reliably estimate the velocity of the vibrating target at a given time during the image collection. If the vibration frequency is all the information that is necessary from a vibrating target, then the *magnitude method* works well, even at low SNR. The *magnitude method* is unable to estimate the frequency of multicomponent or non-stationary sinusoidal vibration.

Chapter 4

Vibration Estimation using the Extended Kalman Filter

4.1 Review of the Kalman Filter

The Kalman Filter, a minimum mean-square error estimator, is a well-established linear estimation technique. Often used in guidance or navigation systems, the Kalman Filter is able to take in noisy data and provide accurate estimates of unknown variables, such as position and velocity. It's popularity is due in part to its computationally efficient algorithm. The Kalman Filter consists of a linear state-transition model and a linear observation model. Both the state-transition model and the observation model must be known a priori in order to provide an accurate state estimation. A recursive algorithm, the Kalman Filter has two distinct steps: prediction step and the correction step. In the prediction step, the state-transition model is used to predict the state variables at the next time step, while the correction step uses the observation model to measure the state variables and update the predicted state estimate. Often, however, the observation is corrupted by noise and the observed

state variables do not reflect the true state variables. This is where the Kalman gain comes into play. The Kalman gain weights how much to trust the system model or the observed states based on the system noise and the observation noise. When the Kalman gain is zero, the algorithm no longer trusts the observations and only trusts the system model. Moreover, when the Kalman gain is 1, the algorithm completely trusts the observations and not the system model. This entire process is optimal when the model matches the real system, the noise is white, and the covariance of the noise is known [14].

In following the section it is shown that the observation model is non-linear with respect to the state variables. This non-linearity makes it impossible to apply the Kalman filter directly as the Kalman Filter was derived by assuming both a linear system and linear observations [14]. However, if the observation model is linearized at each state estimate before applying the Kalman filter, an accurate variable estimation can be achieved. This process is typically called the extended Kalman filter (EKF). While the EKF is generally sub-optimal for nonlinear estimation problems, it is widely used for well-defined transition models and is largely considered the de facto standard in nonlinear estimation [11,23]. The EKF is what is used in the DPCA-SAR SoI for remote vibration estimation.

4.2 The Extended Kalman Filter Model for DPCA-SAR

The EKF filter model discussed here was first proposed by Dr. Wang [24]. To begin, the state vector is defined as,

$$\mathbf{X}_n = (x_v[n], V_v[n])^T, \tag{4.1}$$

where n is each slow time step. Recall, x_v and V_v are the vibrating target's position and velocity in the range direction, respectively. Let $A_v[n]$ denote the instantaneous acceleration, in the range direction, of the vibrating target. A_v can be viewed as an input to the state-transition model. Then, the state-transition model can be written as,

$$\mathbf{X}_{n+1} = \mathbf{F}\mathbf{X}_n + \mathbf{G}A_v[n]. \tag{4.2}$$

where,

$$\mathbf{F} = \begin{pmatrix} 1 & \tau_B \\ 0 & 1 \end{pmatrix} \tag{4.3}$$

and

$$\mathbf{G} = (0, \tau_B)^T. \tag{4.4}$$

In order for this state-transition model to be valid, the input, $A_v[n]$, must be an independent sequence of zero-mean Gaussian vectors. $A_v[n]$ is assumed be an independent sequence of zero-mean Gaussian vectors. Note that the state transition model (4.2) did not make any assumptions about the vibration behavior of the vibrating target other than it must obey Newton's Laws of Motion. Moreover, this model applies for vibrations that increase or decrease in frequency during the collection process. One example of a nonstationary sinusoidal vibration is an engine revving up or down.

Assume, for the moment, a single component sinusoidal vibration. Then the acceleration signal, $A_v[n]$, has the form

$$A(\tau) = A_0 \cos(\omega_0 \tau + \Theta), \tag{4.5}$$

where $\omega_0 = 2\pi f_v$, with f_v being a uniform random variable with support in [1] Θ is a uniform random variable with support in $[-\pi, \pi]$, and A_0 is a uniform random

variable with support in $[0, 2\pi f_v A_v]$, with A_v being the amplitude of the displacement. Then the auto-covariance of $A(t)$ is

$$R_{AA}(\tau) = A_0^2 \cos(2\pi f_v \tau). \tag{4.6}$$

Set $\tau = nT_s$ where T_s is the sampling period. (4.6) is maximized when $2\pi f_0 nT_s = \pi/2$. Recall, the auto-covariance of a Gaussian random variable is a delta function. The auto-covariance of $A(\tau)$ is a symmetrical decaying sinusoid with the apex centered in the middle of the domain. With the appropriate sampling frequency and vibration frequency, R_{AA} approaches a delta function. Therefore, it is not entirely unreasonable to have sinusoidal accelerations be an input to the equation.

The observation model is given by,

$$\begin{aligned} s[n] &= d[n] + w[n] \\ &\equiv h(\mathbf{X}_n) + w[n]. \end{aligned} \tag{4.7}$$

From (2.23), it is clear the observation model is non-linear with respect to the state vector $\mathbf{X}$. To linearize h, take the gradient of h with respect to $\mathbf{X} = (\mathbf{X}(1), \mathbf{X}(2))^T$,

$$\begin{aligned} \nabla h(\mathbf{X}) = \Big(& 4\kappa\overline{\sigma}_v \sin\left(\kappa\tau_B \mathbf{X}(2)\right) e^{j\Phi - j\pi/2}, \\ & 2\kappa\tau_B\overline{\sigma}_v \cos\left(\kappa\tau_B \mathbf{X}(2)\right) e^{j\Phi} - 2\kappa\tau_B\overline{\sigma}_v \sin\left(\kappa\tau_B \mathbf{X}(2)\right) e^{j\Phi - j\pi/2} \Big), \end{aligned} \tag{4.8}$$

where

$$\kappa = \frac{2\pi}{\lambda} \tag{4.9}$$

and

$$\Phi = -k_y y_v n + \phi_v - \kappa(2\mathbf{X}(1) + \tau_B \mathbf{X}(2)) - \frac{\pi}{2}. \tag{4.10}$$

In the EKF, the observation matrix $\mathbf{H}_n$ is defined as

$$\mathbf{H}_n = \nabla h \mid_{\mathbf{X} = \hat{\mathbf{X}}_{n|n-1}}, \tag{4.11}$$

where $\hat{\mathbf{X}}_{n-1}$ is the estimation of $\mathbf{X}_{n-1}$. As such, the linearized observation model can be written as

$$s[n] = \mathbf{H}_n \mathbf{X}_n + w[n], \tag{4.12}$$

$$\begin{aligned}\mathbf{H}_n = \Bigg(& 4\kappa\overline{\sigma}_v \sin\left(\kappa\tau_B \hat{\mathbf{X}}_{n-1}(2)\right) e^{j\Phi - j\pi/2}, \\ & 2\kappa\tau_B\overline{\sigma}_v \cos\left(\kappa\tau_B \hat{\mathbf{X}}_{n-1}(2)\right) e^{j\Phi} - \\ & 2\kappa\tau_B\overline{\sigma}_v \sin\left(\kappa\tau_B \hat{\mathbf{X}}_{n-1}(2)\right) e^{j\Phi - j\pi/2}\Bigg),\end{aligned} \tag{4.13}$$

and

$$\begin{aligned}\Phi_n = -k_y y_v n\Delta t + \phi_v - \frac{2\pi}{\lambda}(2\hat{\mathbf{X}}_{n-1}(1) \\ + \tau_B \hat{\mathbf{X}}_{n-1}(2)) - \frac{\pi}{2}.\end{aligned} \tag{4.14}$$

It is assumed that the variance of the noise $w[n]$ is known. With the state-transition model given in (4.2) and the linearized observation model given in (4.12), the Kalman filter can be used described in [14] and [12] to estimate the vibration dynamics with an initial condition. The solution to the vibration-estimation problem using the Kalman filter is given as follows. Define,

$$s_i^j = (s[i], \ldots, s[j])^T, i < j \text{ and } 0 \leq i, j \leq N. \tag{4.15}$$

Let $\hat{\mathbf{X}}_{n+1|n}$ and $\hat{\mathbf{X}}_{n|n}$ be the predicted and corrected state estimates, respectively. Then the state estimates $\hat{\mathbf{X}}_{n+1|n} \doteq \mathrm{E}[\mathbf{X}_{n+1} \mid s_0^n]$ and $\hat{\mathbf{X}}_{n|n} \doteq \mathrm{E}[\mathbf{X}_n \mid s_0^n]$ are given recursively by,

$$\hat{\mathbf{X}}_{n+1|n} = \mathbf{F}\hat{\mathbf{X}}_{n|n}, n = 1, 2, \ldots \tag{4.16}$$

and

$$\hat{\mathbf{X}}_{n|n} = \hat{\mathbf{X}}_{n|n-1} + \mathbf{K}_n(s[n] - \mathbf{H}_n\hat{\mathbf{X}}_{n|n-1}), n = 1, 2, \ldots \tag{4.17}$$

with the initialization $\hat{\mathbf{X}}_{0|-1} = E[X_0]$. In this thesis it is assumed any vibrating target has symmetrical displacements and velocities with respect to the target's neutral or

static position. Therefore, $\hat{\mathbf{X}}_{0|-1} = E[X_0] = 0$. The Kalman gain, $\mathbf{K}_n$, given by

$$\mathbf{K}_n = \mathbf{\Sigma}_{n|n-1}\mathbf{H}_n^T(\mathbf{H}_n\mathbf{\Sigma}_{n|n-1}\mathbf{H}_n^T + \sigma_w^2)^{-1}, \tag{4.18}$$

where $\mathbf{\Sigma}_{n|n-1} \doteq \mathrm{Cov}(X_n \mid s_0^{n-1})$ and $\mathbf{H}_n^T$ is the transpose of $\mathbf{H}_n$. The covariance matrix, $\mathbf{\Sigma}_{n|n-1}$, can be computed jointly with $\mathbf{\Sigma}_{n|n} \doteq \mathrm{Cov}(X_n \mid s_0^n)$ from the following recursion

$$\mathbf{\Sigma}_{n|n} = \mathbf{\Sigma}_{n|n-1} + \mathbf{K}_n\mathbf{H}_n\mathbf{\Sigma}_{n|n-1}, n = 1, 2, \ldots \tag{4.19}$$

and

$$\mathbf{\Sigma}_{n+1|n} = \mathbf{F}\mathbf{\Sigma}_{n|n} + \mathbf{F}^T\mathbf{G}\mathbf{Q}_n\mathbf{H}^T, n = 1, 2, \ldots \tag{4.20}$$

with the initialization $\mathbf{\Sigma}_{0|-1} \doteq \mathrm{Cov}(X_0)$ where $\mathbf{Q}_n$ is the covariance matrix of the instantaneous vibration acceleration $A_v[n]$. Fig. 4.1 shows the diagram of the Kalman filter for the vibration estimation problem. For a more complete review of the Kalman filter refer to [14] and [20].

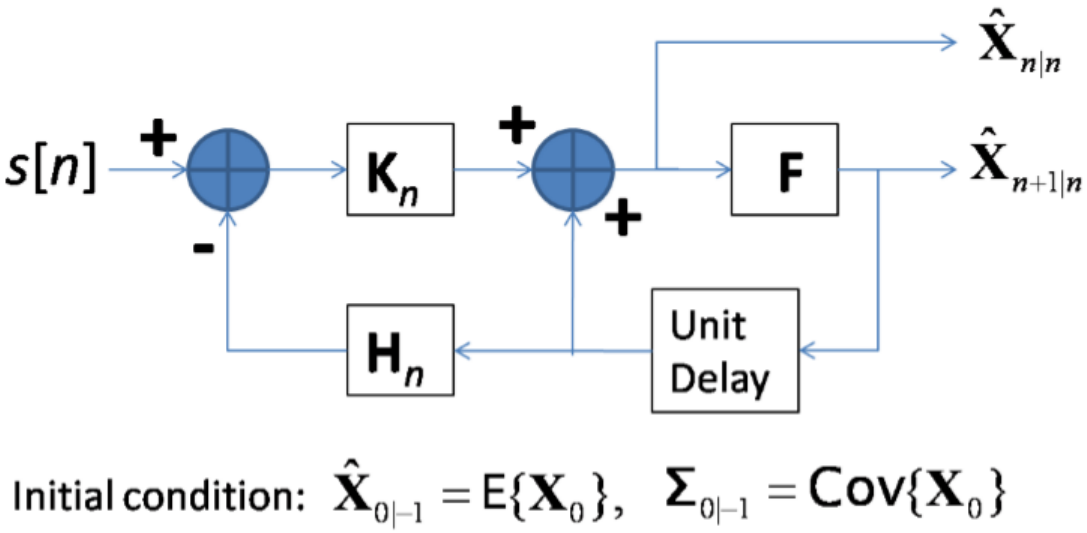

Figure 4.1: Diagram of the Kalman filter for vibration estimation in DPCA-SAR. $s[n]$ is the DPCA-SAR SoI, K_n is the Kalman gain, H_n is the linearized observation matrix, and F_n is the state-transition matrix.

Chapter 5

Observation Noise Immunity by Averaging Over Several State Estimates

5.1 Motivation

Recall, when the state transition model was defined, no assumptions were made about the vibration behavior of the vibrating target other than it must obey the classical laws of motion. Defining the state-transition model in this manner permits the vibration dynamics of the vibrating target to change drastically between each slow-time step. However, while it is not constrained in the state transition model, it was assumed that the PRI was significantly shorter than the period of the vibration of interest. With this assumption, it is not physically possible for the vibration dynamics of the vibrating target to change drastically between each slow-time step. Therefore, any nontrivial changes in the vibration dynamics of the vibrating target in the observed signal, $s[n]$, between successive slow time steps are caused solely by the

observation noise. Since the state transition model does not account for this and since the observations are linearized at each slow-time step, the standard implementation of the EKF is very susceptible to observation noise. This susceptibility to noise can lead to incorrect state-variable estimates and misleading vibration behavior. If the observation noise is suppressed, the EKF becomes much more accurate and stable.

To increase the model's robustness against noise, this thesis proposes averaging over several state estimates to obtain a revised state estimate that more accurately represents the state variables. To motivate this averaging approach, consider, for a moment, a stationary target. Each time this stationary target is observed, the observation noise is going to randomly place this stationary target at the incorrect position in the ground scene. If this stationary object is repeatedly observed over an extended period of time, each observation will create a set of different possible target locations. This set of all observations will be a scattering of locations, centralized and symmetric around the true target location. The centralized and symmetric scattering of observations is because the noise is assumed to be ZMCSCG. As the number of observations get large, the expected value of the set of all the observations will approach the true target location. Thus, resilience to noise is directly related to the number of averaged state estimates.

However, in this thesis, all the targets of interest are vibrating. Thus, averaging over too many state estimates, while suppressing the noise it will also suppress the vibration behavior and only the average target position will remain. Therefore, it is critical to average over as many state estimates as possible to suppress the noise, while not averaging over too many state estimates to ensure retention of the vibration behavior of the target. An analytical expression to determine the number of points to average over is developed below.

If f_v is the vibration frequency of the target of interest, then $\frac{1}{f_v}$ is the time needed for a single complete vibration cycle, or period, M is the number of averaged

points for noise suppression, and Δt is the PRI. Then, the state estimates are being averaged over the time interval, $M\Delta t$. Taking the ratio of these quantities gives the percentage of a single vibration the state estimates are estimated over,

$$\frac{M\Delta t}{\frac{1}{f_v}} = \beta. \tag{5.1}$$

Setting $\beta \approx .125$ insures the average is taken over at most 1/8 of the vibrating period. Averaging over 1/8 or less of the vibrating period appears to ensure the vibration dynamics are not substantially suppressed. This value holds many different target dynamics: sinusoidal and stationary vibrations, sinusoidal and linearly increasing in frequency vibrations, and multicomponent sinusoidal vibrations. These results are shown the *Simulation and Results* section. While any $\beta \leq .125$ is sufficient to retain the vibration behavior, increasing the time of the averaging will increase the noise immunity. Therefore, M should as large as possible, while ensuring $\beta \approx .125$. Or equivalently,

$$M = \max\left\{ n \in \mathbb{N} : n \leq \frac{.125}{\Delta t f_v} \right\}. \tag{5.2}$$

Note that for a given vibration frequency, as the PRF increases (Δt decreases), the number of state estimates that can be averaged, M, increases. Therefore, a higher PRF (low Δt) increases noise immunity for a given target vibration frequency and a given SNR level. Refer to the *Noise Requirements* section and Fig. 5.4 for more information. The improvement of state estimate averaging is shown in Fig. 5.2. Fig. 5.2. is a comparison of the ground truth, applying the EKF directly, and applying the EKF while implementing the state estimate averaging. For a complete description of the state estimate averaging, refer to the *Modification of EKF for Increased Noise Immunity* section.

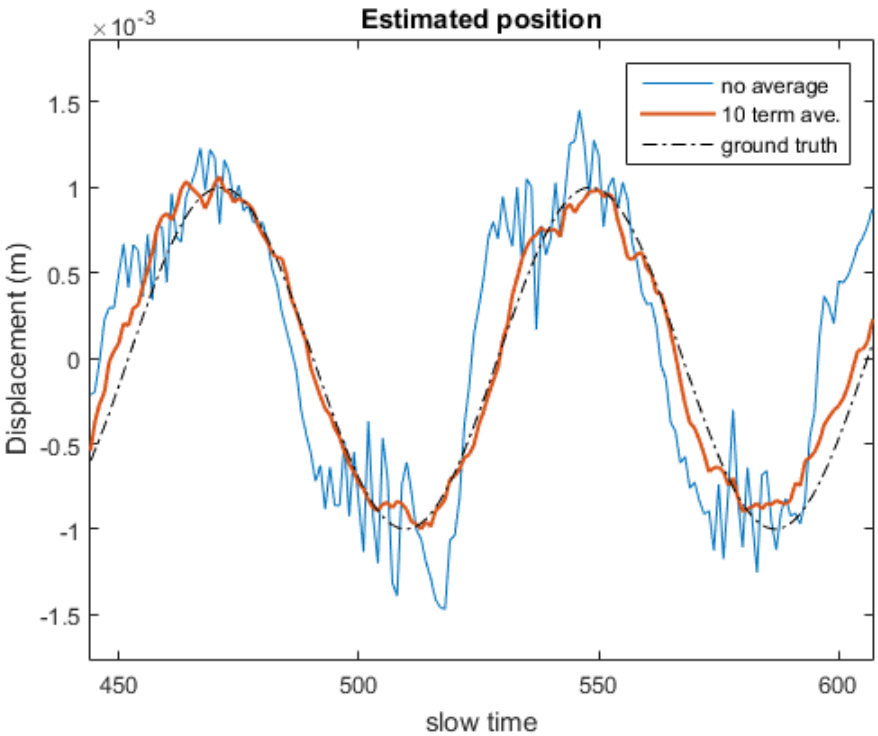

Figure 5.1: Estimated position of a 1 mm, 8 Hz vibrating target using with SNR = 15 dB. State estimate averaging improves the estimated position of the vibrating target significantly when using the EKF based method. More specifically, the MSE is reduced by 34%.

5.2 Determining an Approximate f_v A Priori

One of the potential stumbling blocks of the state estimate averaging method is that it depends on having some a priori knowledge of the vibration frequency of the target of interest. However, this is not an entirely unreasonable assumption. The vibration dynamics of a target are dependent on the material, geometry, and the machinery that is generating the vibrations. If a corporation does remote monitoring of its own systems, it will have access to the material, geometry, and the machinery that is generating the vibrations. Therefore, a range of expected vibration frequencies will be known. If $f_{max(v)}$ is the maximum expected vibration frequency of a given target,

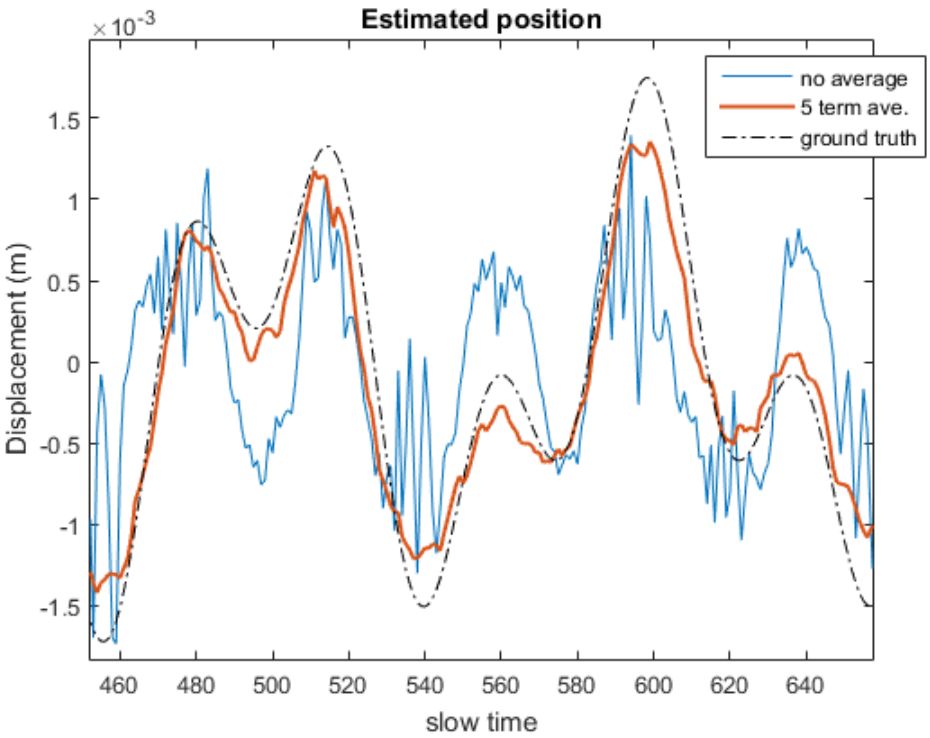

Figure 5.2: Estimated position of a multicomponent vibration. The components are 1 mm, 5 Hz and .75 mm and 12 Hz, with SNR = 15 dB. State estimate averaging improves the estimated position of the vibrating target significantly when using the EKF based method. More specifically, the MSE is reduced by 76%.

then (5.2) can be updated to

$$M = \max\left\{ n \in \mathbb{N} : n \leq \frac{.125}{\Delta t f_{max(v)}} \right\}. \tag{5.3}$$

In other scenarios, the geometry, material, and machinery can sometimes be determined with other remote sensing techniques such as optical, infrared, and multi-spectral, to name a few. Therefore, a maximum expected vibration frequency, $f_{max(v)}$, can be estimated.

Lastly, if working with a single component, sinusoidal vibration, the *magnitude method* could be first used to estimate f_v. Once f_v is determined, then the modified EKF can be applied.

5.3 Modification of EKF for Increased Noise Immunity

Recall, it is the effect of observation noise in the EKF model, rather than the system noise, being mitigated with the state estimate averaging. Thus, the state-transition model, as defined in (4.1), remains unchanged as this is an accurate description for the vibration behavior. Any changes to the state-transition model in an attempt to gain noise immunity would lead to an incorrect state model. In addition, the observation model defined in (4.7) remains unchanged as the DPCA-SAR collection platform has a fixed imaging procedure that cannot be altered. The modification occurs in the linearization of the observation model, as it is the linearization that is susceptible to the observation noise.

As described in the EKF section, the observation matrix, $\mathbf{H}_n$, is defined as

$$\mathbf{H}_n = \nabla h \mid_{\mathbf{X}=\hat{\mathbf{X}}_{n|n-1}}, \tag{5.4}$$

where $\hat{\mathbf{X}}_{n|n-1}$ is the estimation of $\mathbf{X}_n$. In addition, the initialization of the state estimates is $\hat{\mathbf{X}}_{0|-1} = E[X_0]$.

Now, let N_1 be the total number of state estimates being averaged, where N_1 is determined by (5.2). Then the observation matrix, $\mathbf{H}_n$, is now defined as

$$\mathbf{H}_n = \nabla h \mid_{\mathbf{X}=\hat{\mathbf{X}}_{ave(n)}}, \tag{5.5}$$

where

$$\hat{\mathbf{X}}_{ave(n)} = \frac{\hat{\mathbf{X}}_{n|n-1} + \hat{\mathbf{X}}_{n-1|n-2} + \cdots + \hat{\mathbf{X}}_{n-N_1+1|n-N_1}}{N_1}. \tag{5.6}$$

Then, the initialization of the state estimates are

$$\hat{\mathbf{X}}_{N_1-1|N_1-2} = \cdots = \hat{\mathbf{X}}_{1|0} = \hat{\mathbf{X}}_{0|-1} = E[X_0] = 0. \tag{5.7}$$

This is the sole location in the EKF algorithm that an average of state estimates is used to provide noise immunity. The remainder of the EKF algorithm remains as defined from (4.12) to (4.20). A comparison of the linearizied state observation with state estimate averaging and without state estimate averaging are shown in Fig. 6.2 and Fig. 6.1, respectively.

5.4 Noise Requirements

One of the potential challenges when implementing the EKF is that under certain conditions, the state estimations provided through the EKF algorithm can diverge from the actual state variables. This divergence is typically caused by the estimated state error covariance matrix becoming extremely and unrealistically small. When the covariance matrix is very near to zero, the Kalman Gain places unreasonable trust in the state prediction and ignores subsequent observations [9]. When this occurs, the vibrational dynamics of targets cannot be reliably determined. Therefore, for accurate vibrometry, it is necessary to characterize the pervasiveness of this divergence and determine how to reduce the divergence to negligible levels.

An example of what happens to the state estimate when the estimated state error covariance becomes unrealistically small is shown in Fig. 5.3. It is clear that EKF no longer trusts the observations and the vibrating target's state estimates are updated only using the predicted state estimate from the state transition model.

For the noise characterization, the vibrating target is assumed to have a steady (constant frequency) sinusoidal motion of 8 Hz with a 1 mm displacement. The system parameters used for this characterization are described in Table 6.1. For further explanation refer to the *Simulations and Results* section. With these target dynamics, 1,000 simulated slow-time DPCA-SAR SoIs were generated. Each realization of the slow-time signal was corrupted with ZMCSCG noise. Then, the aforementioned

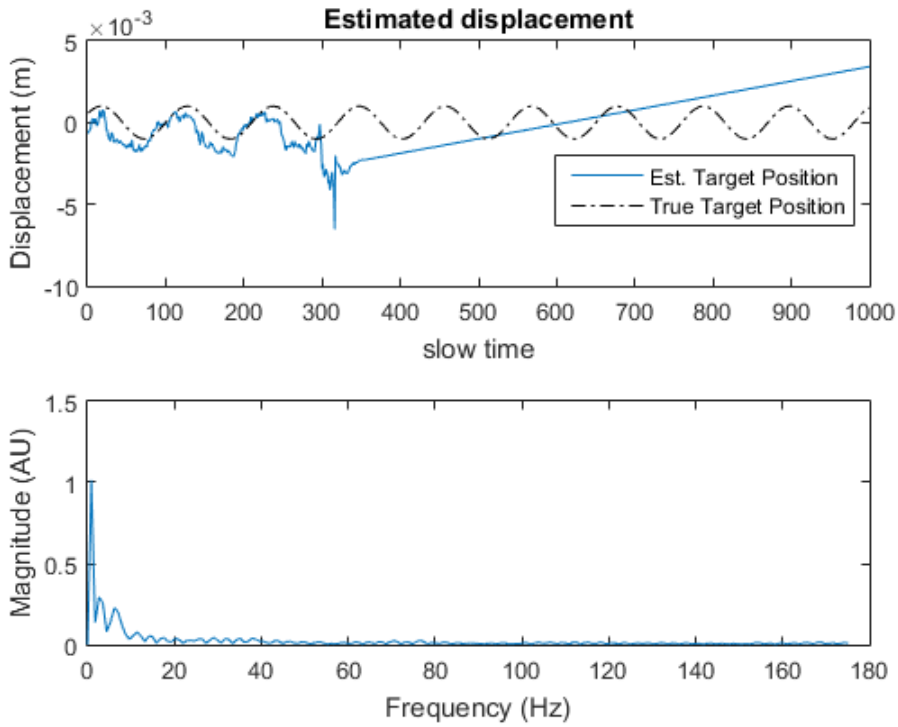

Figure 5.3: Estimated position and estimated frequency of a 1 mm, 8 Hz vibrating target using the EKF with SNR = 11 dB. Strong successive noisy observations cause the Kalman gain to place unreasonable trust in the predicted state estimates and not trust the observations.

EKF method was applied to each slow-time signal. If *EKF method* reliably estimated the frequency of the vibrating target within 1 Hz, the estimation was considered to have converged. Otherwise, the method was considered to have diverged. The ratio of converging solutions to the total number of slow-time SoI was taken. This process was repeated for integer SNR values ranging from 1 to 15. The SNR is defined as

$$SNR = 10 \log_{10} \left(\frac{\sigma}{\sigma_w} \right), \tag{5.8}$$

where σ_w^2 is variance of the observation noise. This entire procedure was done with the averaging for noise immunity method and without the averaging for noise immunity method. The results are shown in Fig. 5.4.

Table 5.1: Performance Limits of the *EKF method* DPCA-SAR Vibration Estimation

parameter	quantity
Required SNR	15 dB
Frequency Resolution	$\frac{1}{f_{prf}N}$
MMVV	$\frac{\lambda}{4\tau_B}$
MMVF	theoretically $\frac{f_{prf}}{2}$; with state averaging $\frac{f_{prf}}{2N_1}$

Fig. 5.4 shows for a given SNR level, the state estimate averaging for noise immunity increases the occurrence of converging solutions. For example, when the SNR = 8 dB, diverging solutions occur 60% less often when the state estimates are averaged compared without any state estimate averaging. Therefore, for the minimal computational effort, averaging provides not only increased confidence in vibration behavior, but also decreases the likelihood of a diverging solution when SNR $<$ 15 dB. When the SNR exceeds 15 dB, it appears divergence is no longer a concern.

5.5 Signal to Clutter Ratio

In a general sense, clutter can be defined as the collection of all targets or objects that engender undesired reflections in the radar's return signal. These undesired reflections often degrade the performance of the radar system as the target of interest cannot be separated from the background. Clutter can be placed into one of two categories: surface clutter and airborne clutter. Some examples of surface clutter include vegetation, ground terrain, ocean surface condition, and jungle canopies. Airborne clutter, sometimes termed volume clutter, typically refers to rain, insects, or birds. In this study, only ground clutter is considered. Since the SAR system is designed to be an all weather imaging system, the majority of airborne clutter only has negligible affects on the quality of the SAR image.

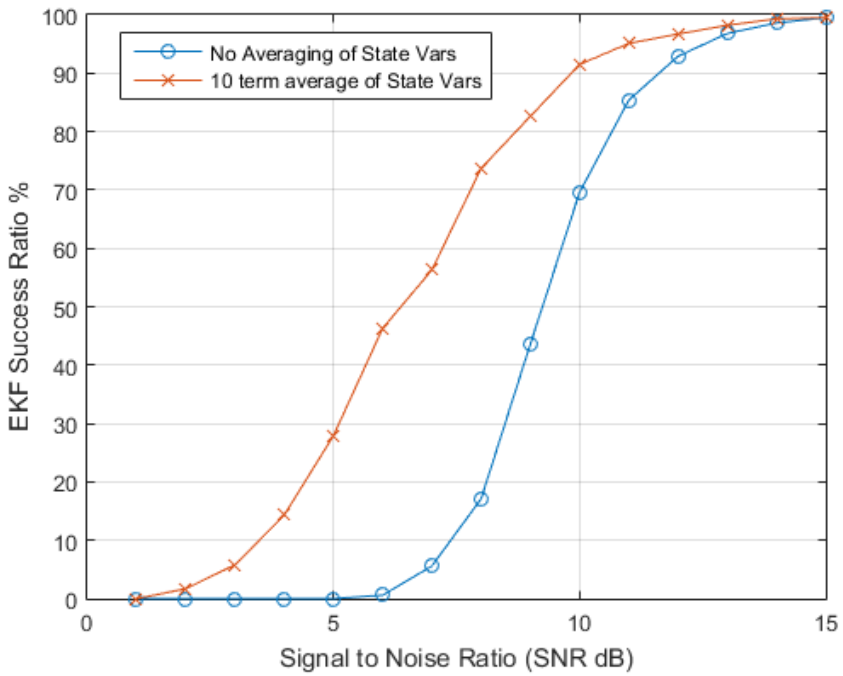

Figure 5.4: Estimated position and estimated frequency of a 1 mm, 8 Hz vibrating target using the EKF with SNR = 11 dB.

Recall, one of the distinct advantages of the DPCA-SAR systems is that it performs quite well when introduced into a high clutter environment. In real-world applications, the removal of the clutter signal is subject to the noise floor of the DPCA-SAR system [5]. When the noise increases, uncanceled or residual clutter will be present. However, this residual clutter will be indistinguishable from the noise signal. This noise is generated from any incoherence between the two antennas, in addition to the thermal noise. This incoherence is generated from a variety of imperfections in the collection platform, as well as natural background radiation.

One example that causes the stated incoherence are imperfections in the flight path. Often the collection flight path is irregular due to turbulence. This irregular flight path causes the aft antenna to be in a slightly different collection location than the fore antenna. This causes the differing clutter signals between antennas and

some clutter cannot be canceled. On board the there typically is a GPS and some type of inertial measurement unit (IMU) or guidance system. These systems track the position of the collection platform for the duration of the flight. The GPS and IMU typically help to compensate for the irregular flight path, however their success is limited by their own error margins. Since turbulence can be viewed as a random process and the GPS and IMU errors are random, this incoherence can be viewed as noise.

A second example that causes incoherence are inconsistencies between the fore and aft antennas. Any misalignments in phase result in a corresponding range error. With the same clutter signal mapped to a different range line for each antenna, there is no way these clutter signals can be removed. Since this phase error is due to real world system limitations, it is random and can also be viewed as noise.

Therefore, the clutter can only be canceled down to the noise level. Therefore, the DPCA-SAR signal of interest to residual clutter ratio (SCR) is for all intents and purposes equivalent to the signal to noise ratio. The SCR may in fact be worse than the SNR. However, the SCR cannot be better than the SNR.

Chapter 6

Simulations and Results

The proposed method in this thesis is validated by simulating the DPCA-SAR SoI (the returned observed SAR difference signal) in MATLAB. The simulated DPCA-SAR system is operating in the K_u-band. All of the key system parameters are listed in Table 6.1. These system parameters are chosen in part to mimic the Lynx radar [21]. The baseline, B and the platform velocity, V_a are, however, notional values of a DPCA-SAR system. The DPCA-SAR SoI was generated using the model defined in (2.21) and (2.23).

6.1 Sinusoidal Vibration Simulation

For the first set of simulations, consider a vibrating target whose displacement is described through a sinusoidal vibration of a constant frequency. The target had a 8 Hz oscillation with an amplitude of 1 mm. Fig. 6.1 shows the results of the *EKF method* estimating the position of a vibrating target without using the state estimate averaging technique described in the *Observation Noise Immunity By Averaging Over Several State Estimates* section. Fig. 6.2 show the results of the *EKF method* esti-

Table 6.1: DPCA-SAR System Parameters Used In Simulations

parameter	quantity
center frequency	16 GHz
effective PRF	487 Hz
propagation velocity	3×10^8 m/s
platform velocity	175 m/s
slant range	10 km
azimuth resolution	.33 m
aperture length	363 m
SNR	15 dB
Baseline	0.3596 m

mating the position of a vibrating target with the state estimate averaging. In this case, the state estimate averaging occurred over 10 consecutive terms. It is clear from the Fig. 6.2 that the state estimate average improves the position estimate of the vibrating target and more energy is localized for the estimated frequency.

6.2 Linearly Increasing Frequency Vibration

For the next set of simulations, consider a vibrating target whose displacement is described through a sinusoidal vibration that linearly increases in frequency throughout the duration of the aperture. The target oscillations began at 10 Hz and linearly increased to 17 Hz. The target's displacement was set to 1 mm. The position estimation for the linear increasing vibration is show in Fig. 6.3. As with the constant frequency sinusoidal vibration, after about two complete oscillations the estimated target position converges to the true target position.

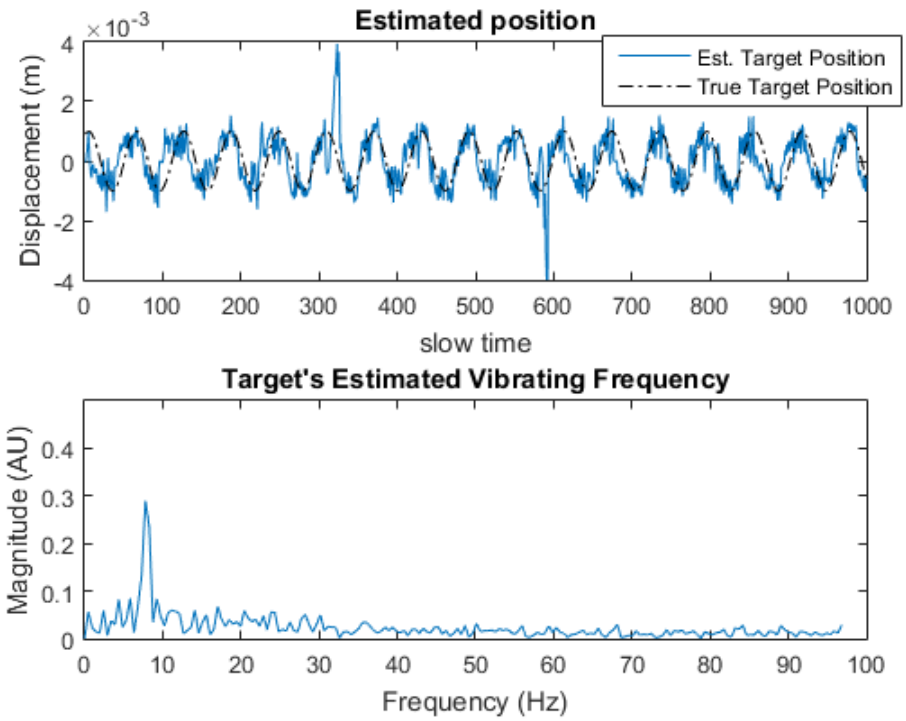

Figure 6.1: Estimated position and estimated frequency of a 1 mm, 8 Hz vibrating target using the EKF with SNR = 15 dB.

6.3 Linearly Decreasing Frequency Vibration

Now consider a vibrating target whose displacement is described through a sinusoidal vibration that linearly decreases in frequency throughout the duration of the aperture. The target oscillations began at 16 Hz and linearly decreased to 8 Hz. The target's displacement was set to 1 mm. The position estimation for the linear increasing vibration is shown in Fig. 6.4. Again, after approximately two oscillations the estimated position of the vibrating target converges to the true target position.

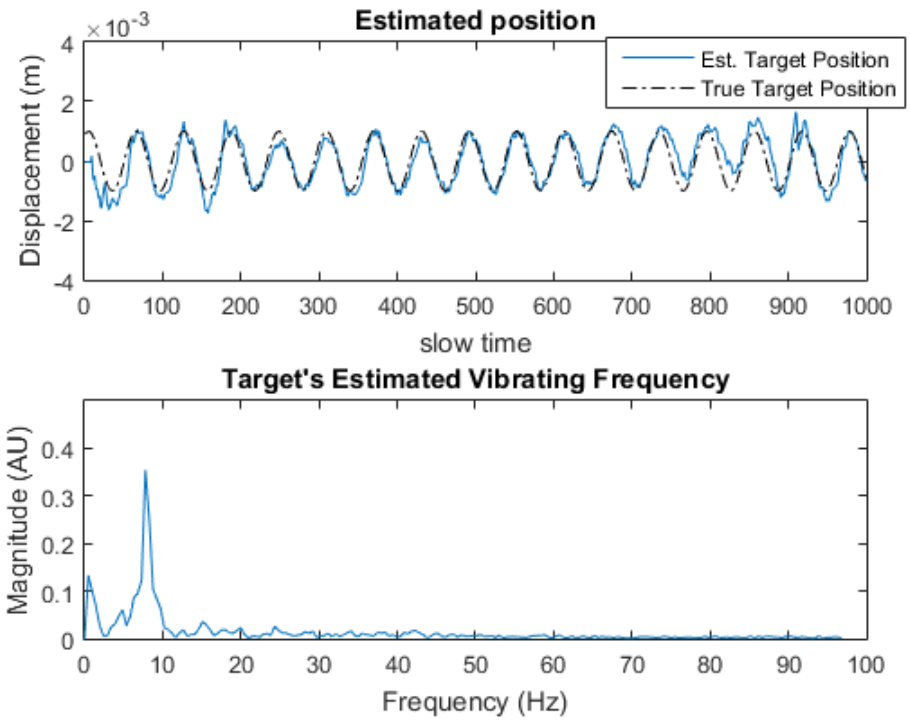

Figure 6.2: Estimated position and estimated frequency of a 1 mm, 8 Hz vibrating target using the EKF with SNR = 15 dB. The state estimates were linearized over 7 terms for noise suppression.

6.4 Multicomponent Vibration

Lastly, consider a vibrating target whose displacement is described as a superposition of two sinusoids. The first frequency component has a 5 Hz vibration frequency with a displacement of 1 mm. The second frequency component has a 12 Hz vibration frequency with a displacement of .75 mm. The position estimation for the multicomponent vibration without state estimate averaging is shown in Fig. 6.5. The position estimation for the multicomponent vibration with state estimate averaging is shown in Fig. 6.6. Fig. 6.6 shows that state estimate averaging is required for accurate position estimation of the vibrating target. Even with the additional vibration component, the estimated position closely matches the true target position.

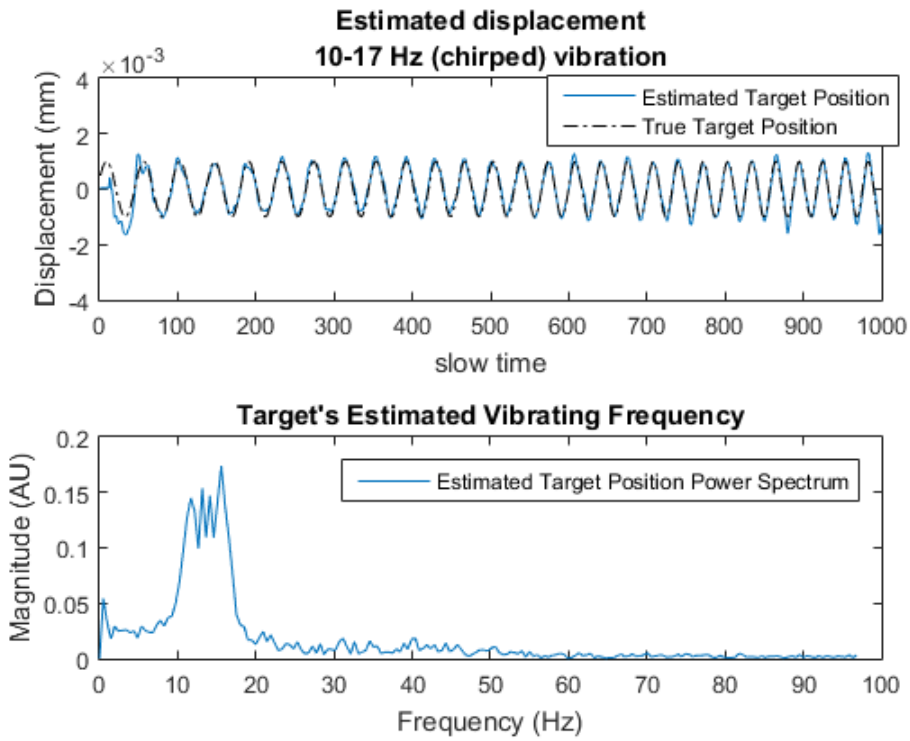

Figure 6.3: Position Estimation using EKF of a target's vibration frequency increasing linearly from 10 Hz to 17 Hz. The amplitude of the vibration was 1 mm. The state estimates were linearized over 10 terms for noise suppression.

Since the highest frequency component is 12 Hz, the state estimates are averaged over 5 consecutive terms.

6.5 Results

The modified *EKF method* has the ability to estimate not only a vibrating target's frequency, but it can also determine its position and velocity at any given time during the collection process. The modified *EKF method* is no longer restricted to a signal component, sinusoidal vibration. It is now possible to accurately track the position of the target for multicomponent vibrations. In addition, the modified *EKF method*

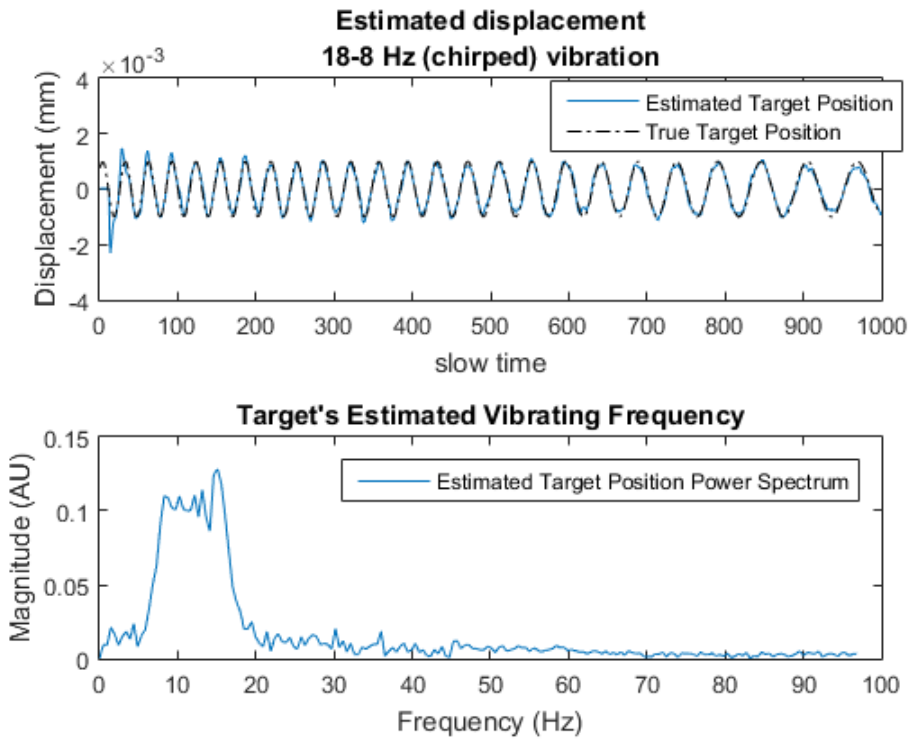

Figure 6.4: Position Estimation using EKF of a target's vibration frequency decreasing linearly from 16 Hz to 8 Hz. The amplitude of the vibration was 1 mm. The state estimates were linearized over 10 terms for noise suppression.

presented here works for vibrations that increase linearly or decrease linearly during the collection process. The success was highly dependent on implementing the state estimate averaging. The mean square error (MSE) of the original method is .2279, while the MSE of the method presented in this paper is .1503. Therefore, the method presented in this paper improves the position estimate of the vibrating target by 34% when SNR = 15 dB. For the multicomponent vibrations, the mean square error of the estimated target position is reduced by 76% when SNR = 15 dB.

In addition, the state estimate averaging technique decreased the likelihood of the EKF solution from diverging from the true position of the vibrating target. When the SNR = 8 dB, this divergence was decreased by 60%.

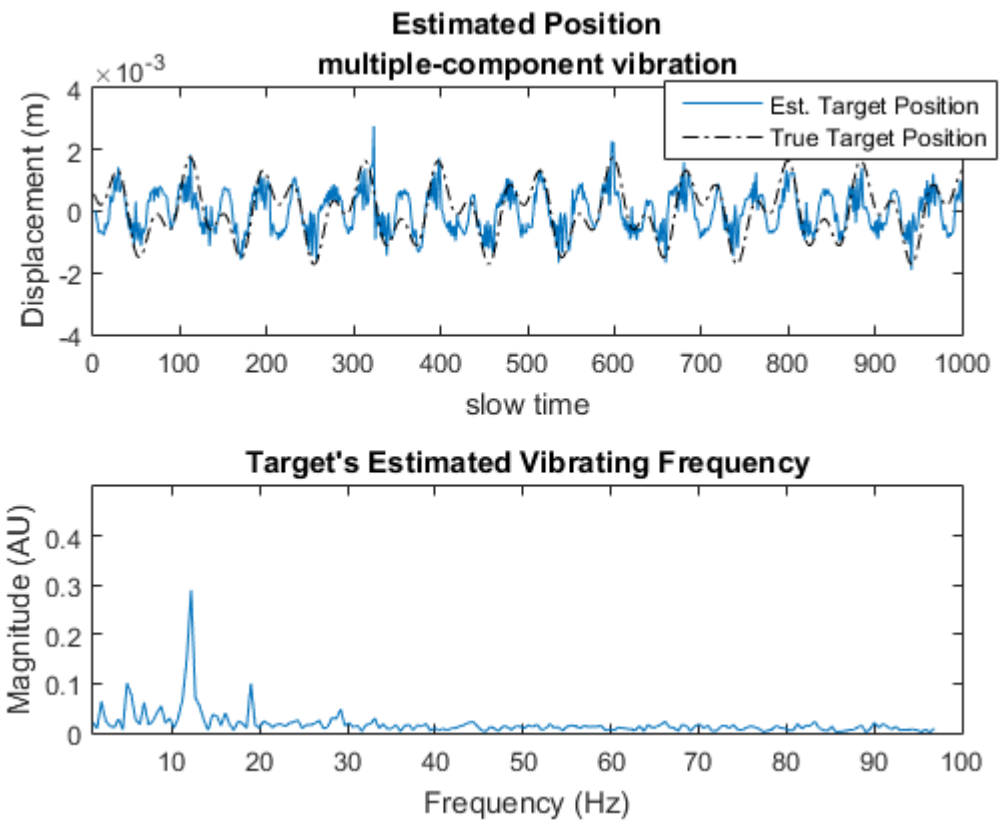

Figure 6.5: Position Estimation using EKF of a target's multicomponent vibration frequency of 5 Hz and 12 Hz. No state estimate averaging. SNR = 15 dB.

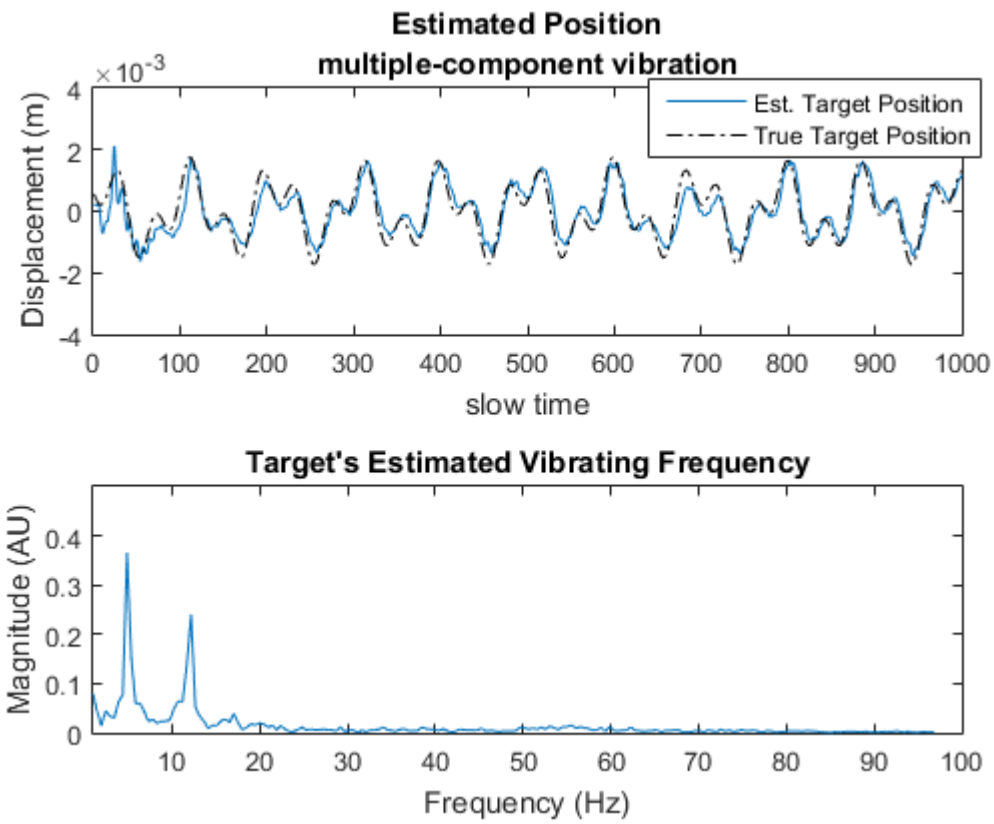

Figure 6.6: Position Estimation using EKF of a target's multicomponent vibration frequency of 5 Hz and 12 Hz. 5 state estimate terms were averaged. SNR = 15 dB.

Chapter 7

Conclusion

SAR is a universally accepted remote sensing platform that is used for a variety of applications. Typically, SAR produces a high-resolution, two-dimensional image of a scene of interest. An underlying assumption when creating this high resolution image is that all targets in the ground scene are stationary. If a target is not static, but instead vibrating, it introduces a modulation on the returned radar signal termed the micro-Doppler effect. The ability to estimate the target's vibration frequency and vibration amplitude by exploiting the micro-Doppler effect, all while in a high clutter environment can provide strategic information for target identification and target condition/status. This thesis improved one method that processes the non-stationary signal of interest generated by the vibrating target in DPCA-SAR in high clutter.

This thesis began by introducing some of the basic processing performed in SAR. After the basic signal processing techniques are established, the DPCA-SAR is introduced. It is then demonstrated how DPCA-SAR works particularly well in a high clutter environment and how this technique can be exploited.

Then the *magnitude method*, first developed by Dr. Wang [24] is introduced for

context and motivation for the *EKF method*. For a single component, sinusoidal vibration, the *magnitude method* can estimate the frequency of the vibrating target when the SNR is greater or equal to 4 dB. The *magnitude method*, however, could not estimate the velocity or position of the vibrating target at any time during the collection process. The *magnitude method* cannot be expanded to more complex vibrations, such as multicomponent vibrations or vibrations that evolve over time.

After the *EKF method* was given, a modified version of the *EKF method* is presented. This modification implemented a state estimate averaging technique when linearizing the observation function of the EKF algorithm. This state estimate averaging technique, while computationally inexpensive, made a profound impact on the performance of the *EKF method.*

The modified *EKF method* is capable of estimating not only a vibrating target's frequency, but it could also determine its position and velocity at any given time during the collection process. The modified *EKF method* is no longer restricted to a signal component, sinusoidal vibration. It can now accurately track the position of the target for multicomponent vibrations. In addition, the modified *EKF method* presented here works for vibrations that increase linearly or decrease linearly during the collection process. The success was highly dependent on implementing the state estimate averaging. The mean square error (MSE) of the original method is .2279, while the MSE of the method presented in this paper is .1503. Therefore, the method presented in this paper improves the position estimate of the vibrating target by 34% when SNR = 15 dB. For the multicomponent vibrations, the mean square error of the estimated target position is reduced by 76% when SNR = 15 dB. Finally, the state estimate averaging technique decreased the likelihood of the EKF solution from diverging from the true position of the vibrating target. When the SNR = 8 dB, this divergence was decreased by 60%.

Chapter 8

Future Work

The next steps for these techniques is to test and validate them on a real world SAR system such as the Lynx SAR system operated by General Atomics-Aeronautical Systems Inc. To make this a possibility, the University of New Mexico's Radar Vibrometry Team would have to have access to GA-ASI engineering system as this technique cannot be directly applied to current standard production systems. The Radar Vibrometry Team is currently looking at imaging the Ford Utility Building on main campus. The Ford Utility Building provides electricity, cooling, and hot water across main and north campus. This facility had a variety of vibrating ventilation stacks placed inside a high clutter environment. After acquiring the vibrating dynamics of the individual vent stacks, the team will try to identify which machinery is operating inside the Ford Utility Building.

Appendices

A MATLAB Code for Magnitude Method

B MATLAB Code for EKF Method

Appendix A

MATLAB Code for Magnitude Method

The *magnitude method* for Single Component Vibration

15 June 2016, UNM RADAR Vibrometry, JBC

Here the *magnitude method* is used for remote vibration estimation of a single vibrating target in a simulated SAR image. It is assumed that all clutter is removed in this simulation by exploiting the dual beam antenna. There is, however, white noise that is added to the SoI.

Contents

- Target's Vibration information
- Simulating the observations
- Plot Dual-Beam SoI
- Target's vibration frequency estimation from SoI
- Estimate position from estimated frequency

Begin Program

```
clc;
clear;
close all;
```

Initializing Parameters

```
fc = 1.6e10;            % Center frequency
c = 3e8;                % Propagation Velocity
lambda_c = c / fc;      % Wavelength
V = 175;                % Platform Velocity (meters)
Rc = 10000;             % Range to image center (meters)
N = 1000;               % Number of samples
rhoy = 0.33;            % Azimuth res
diameter.y = rhoy * N;  % Azimuth physical size
%ka = 1.58;             % Armin reference (effective prf paper
ka = 2;
prf = V*ka*diameter.y/(lambda_c*Rc);    % Pulse Repetition Frequency
ts = 1 / prf;           % PRI (pulse repetition interval)

% Frequently used constants
```

```
PI2 = pi * 2;
PI4 = pi * 4;

PI2_lambda = PI2 / lambda_c;
PI4_lambda = PI4 / lambda_c;

ky = (PI4*fc*V)/(c*Rc*prf); % scaling parameter
```

Target Information

```
tgt.sigma = 1e-4;       % Reflectance magnitude
tgt.y = 3;              % Azmmith Position
tgt.phi = 0.1 * pi;     % Initial phase

% Total Reflectance
tgt_phs_ref = -ky * tgt.y * (1:N) + tgt.phi; %
tgt_ref = tgt.sigma * exp(1j * tgt_phs_ref); %
```

Target's Vibration information

```
vib.amp = 1e-3;             % 1 mm vibration amplitude
vib.frq = 8;                % vibration frequency of 8 Hz
vib.phi = 0;                % zero initial vibration displacement
vib.y = 0 + diameter.y / 2; % target postion
M_b = 10;                   % SAR carrier baseline
t_b = M_b * ts;             % time delay between two antennas
st = (1:N) * ts + t_b;      % timing of pulses
```

```
vib_dis = vib.amp * sin(PI2 * vib.frq * (st) + vib.phi);
vib_vlc = vib.amp * PI2 * vib.frq * cos(PI2 * vib.frq * (st) + vib.phi);

% figure(01010)
% subplot(2,1,1)
% plot(vib_dis);
% xlabel('slow time');
% ylabel('Displacement (mm)');
% title('Sinusodal Target Vibration-Displacement');
% subplot(2,1,2)
% plot(vib_vlc);
% xlabel('slow time');
% ylabel('Velocity (mm/s)');
% title('Sinusodal Target Vibration-Velocity');
```

Simulating the observations

```
soi_dualbeam = zeros(N,1);

for i = 1:N
    tau = i * ts;
    dis2 = vib.amp * sin(PI2 * vib.frq * (tau+t_b) + vib.phi);
    dis1 = vib.amp * sin(PI2 * vib.frq * (tau) + vib.phi);
    soi_dualbeam(i) = tgt_ref(i) * (exp(-1j* PI4_lambda * dis2) - ...
        exp(-1j* PI4_lambda * dis1));
end

% figure(9999)
```

```
% plot(imag(soi_dualbeam))
% hold on
% soi_dualbeam_pure = soi_dualbeam;
% xlabel('slow time');
% ylabel('Magnitude (AU)');
% title('DPCA-SAR Signal of Interest');

snr = 4;                                % Signal to Noise Ratio
var_w = tgt.sigma^2 / 10^(snr/10);  % variance of the noise (def of SNR)
w = sqrt(var_w/2) * randn(N,1) + 1j * sqrt(var_w/2) * randn(N,1);
                                        % Complex valued white Gaussian noise
soi_dualbeam = soi_dualbeam + w;
```

Plot Dual-Beam SOI

```
figure(10)
subplot(2,1,1)
plot(abs(soi_dualbeam));
xlabel('slow time');
ylabel('Magnitude (AU)');
title('DPCA-SAR Signal of Interest');

subplot(2,1,2)
est_spc_mag = abs(fft(abs(soi_dualbeam)-mean(abs(soi_dualbeam))));
spc_upper = 200;
plot((0:spc_upper-1)/N*prf, est_spc_mag(1:spc_upper));
xlabel('Frequency (Hz)');
ylabel('Magnitude (AU)');
```

Target's vibration frequency estimation from SoI

```
zulu2 = est_spc_mag(1:spc_upper)';
[alpha3,bravo3] = max(zulu2);
charlie2 = (0:spc_upper)/N*prf;
est_frq1 = charlie2(bravo3);
est_frq1 = est_frq1/2;
zulu2(:,bravo3) = 0;
[alpha4,bravo4] = max(zulu2);
est_frq2 = charlie2(bravo4);
est_frq2 = est_frq2/2;
if abs(bravo3-bravo4) < 4
   tot_est_frq = (est_frq1 + est_frq2)/2;
else
    if alpha3>alpha4
        tot_est_frq = charlie2(bravo3);
        tot_est_frq = tot_est_frq/2;
    else
        tot_est_frq = charlie2(bravo4);
        tot_est_frq = tot_est_frq/2;
    end
end
disp('Target''s estimated vibration frequency from postion estiamtes: ')
disp(tot_est_frq)


Target's estimated vibration frequency from postion estiamtes:
    8.0080
```

Estimate position from estimated frequency

```
est_vlc = asin(soi_dualbeam/(2*tgt.sigma))*((lambda_c)/(2*pi*t_b));
est_vlc = est_vlc - mean(est_vlc);
figure
plot(imag(est_vlc))
hold on;
plot(vib_vlc,'k-.');
xlabel('slow time');
ylabel('Velocity (mm/s)');
title({'Estimated velocity of a 1 mm, 8 Hz vibrating target', ...
       'using the \textit{magnitude method} with SNR = 4 dB'})
legend('Est. Target Velocity', 'True Target Velocity')

%[b,a] = butter(6,0.073,'low');
%[b,a] = cheby1(6,10,0.073,'low');
[b,a] = cheby2(6,10,0.08,'low');
dataIn = est_vlc;
dataOut = filter(b,a,dataIn);
dataOut = dataOut - mean(dataOut);

figure
plot(imag(dataOut))
hold on;
plot(vib_vlc,'k-.');
xlabel('slow time');
ylabel('Velocity (mm/s)');
title({'Estimated velocity of a 1 mm, 8 Hz vibrating target', ...
```

```
        'using the \text{magnitude method}with SNR = 4 dB'})
legend('Est. Target Velocity', 'True Target Velocity')
```

Appendix B

MATLAB Code for EKF Method

The Extended Kalman Filter Single Component Vibration

18 November 2015, UNM RADAR Vibrometry, JBC

Here the extended Kalman filter is used for remote vibration estimation of a single vibrating target in a simulated SAR image. It is assumed that all clutter is removed in this simulation by exploiting the dual beam antenna. There is, however, white noise that is added to the SoI.

First written by Qi Wang: 11 July 2012

Contents

- Initializing Parameters
- Target Information
- Target's Vibration information
- Simulating the observations
- Plot Dual-Beam SoI
- Start the Kalman Filtering
- In these simulations we assume the prf is significantly faster than the
- State equation parameters.
- Estimated Velocity
- Plot estimated position
- Target's vibration frequency estimation from position estiamtes

Begin Program

```
clc;
clear;
close all;
```

Initializing Parameters

```
fc = 1.6e10;            % Center frequency
c = 3e8;                % Propagation Velocity
lambda_c = c / fc;      % Wavelength
V = 175;                % Platform Velocity (meters)
Rc = 10000;             % Range to image center (meters)
N = 1000;               % Number of samples
rhoy = 0.33;            % Azimuth res
diameter.y = rhoy * N;  % Azimuth physical size
```

```
ka = 1.58;              % Armin reference (effective prf paper)
%ka = 2;
prf = V*ka*diameter.y/(lambda_c*Rc);    % Pulse Repetition Frequency
ts = 1 / prf;           % PRI (pulse repetition interval)

% Frequently used constants
PI2 = pi * 2;
PI4 = pi * 4;

PI2_lambda = PI2 / lambda_c;
PI4_lambda = PI4 / lambda_c;

ky = (PI4*fc*V)/(c*Rc*prf); % scaling parameter
```

Target Information

```
tgt.sigma = 1e-4;       % Reflectance magnitude
tgt.y = 3;              % Azmmith Position
tgt.phi = 0.1 * pi;     % Initial phase

% Total Reflectance
tgt_phs_ref = -ky * tgt.y * (1:N) + tgt.phi; %
tgt_ref = tgt.sigma * exp(1j * tgt_phs_ref); %
```

Target's Vibration information

```
vib.amp = 1e-3;             % 1 mm vibration amplitude
vib.frq = 8;                % vibration frequency of 8 Hz
```

```
vib.phi = 0;                % zero initial vibration displacement
vib.y = 0 + diameter.y / 2; % target postion
M_b = 10;                   % SAR carrier baseline
t_b = M_b * ts;             % time delay between two antennas
st = (1:N) * ts + t_b;      % timing of pulses

vib_dis = vib.amp * sin(PI2 * vib.frq * (st) + vib.phi);
vib_vlc = vib.amp * PI2 * vib.frq * cos(PI2 * vib.frq * (st) + vib.phi);

% figure(01010)
% subplot(2,1,1)
% plot(vib_dis);
% xlabel('slow time');
% ylabel('Displacement (mm)');
% title('Sinusodal Target Vibration-Displacement');
% subplot(2,1,2)
% plot(vib_vlc);
% xlabel('slow time');
% ylabel('Velocity (mm/s)');
% title('Sinusodal Target Vibration-Velocity');
```

Simulating the observations

```
soi_dualbeam = zeros(N,1);

for i = 1:N
    tau = i * ts;
    dis2 = vib.amp * sin(PI2 * vib.frq * (tau+t_b) + vib.phi);
```

```
    dis1 = vib.amp * sin(PI2 * vib.frq * (tau) + vib.phi);
    soi_dualbeam(i) = tgt_ref(i) * (exp(-1j* PI4_lambda * dis2) - ...
        exp(-1j* PI4_lambda * dis1));
end

% figure(9999)
% plot(imag(soi_dualbeam))
% hold on
% soi_dualbeam_pure = soi_dualbeam;

snr = 11;                              % Signal to Noise Ratio
var_w = tgt.sigma^2 / 10^(snr/10);  % varance of the noise (def of SNR)
w = sqrt(var_w/2) * randn(N,1) + 1j * sqrt(var_w/2) * randn(N,1);
                                       % Complex valued white Gaussian noise
soi_dualbeam = soi_dualbeam + w;
```

Plot Dual-Beam SOI

```
figure(10)
subplot(2,1,1)
plot(abs(soi_dualbeam));
xlabel('slow time');
ylabel('Magnitude (AU)');
title('DPCA-SAR Signal of Interest');

subplot(2,1,2)
est_spc_mag = abs(fft(abs(soi_dualbeam)-mean(abs(soi_dualbeam))));
spc_upper = 200; %??
```

```
plot((0:spc_upper-1)/N*prf, est_spc_mag(1:spc_upper));
xlabel('Frequency (Hz)');
ylabel('Magnitude (AU)');
```

Start the Kalman Filtering

```
X = zeros(2,1,N+1);     % State of the vibrating target [ pos., vel. ]
Y = soi_dualbeam;       % Observation (range compressed slow time signal)

EX = zeros(2,1,N);      % State estimate (correction)
PX = zeros(2,1,N+5);    % State prediction
MPX = zeros(2,1,N+1);   % State prediction average over several pulses

CEX = zeros(2,2,N);                % system error covariance (correction)
CPX = zeros(2,2,N+1);              % system error covariance (prediction)
%X(:,:,1) = [0;vib.amp*vib.frq*PI2]; % the initial target state ...
X(:,:,1) = [0;0];                  % the initial target state ...
PX(:,:,1) = X(:,:,1);
```

In these simulations we assume the prf is significantly faster that the

target's vibration fequency. Therefore, the target's state (position, velocity) will remained relatively unchanged between several successive pulses. Therefore, I intialize the first couple of terms with the same values.

Position is kinda orthogonal to velocity. Recall target displacement is 1 mm

```
cvp = 1e-6/2;                  % co-variance of the target position
```

```
cvv = cvp * PI2^2 * (vib.frq)^2;% co-variance of the target velocity        deriva
CPX(:,:,1) = [cvp, 0; 0, cvv];  % co-variance of the intial vib. pos.
CPX(:,:,2) = CPX(:,:,1);
CPX(:,:,3) = CPX(:,:,1);
CPX(:,:,4) = CPX(:,:,1);
CPX(:,:,5) = CPX(:,:,1);
CPX(:,:,6) = CPX(:,:,1);
CPX(:,:,7) = CPX(:,:,1);
CPX(:,:,8) = CPX(:,:,1);
CPX(:,:,9) = CPX(:,:,1);
CPX(:,:,10) = CPX(:,:,1);
var_u = cvp * PI2^4 * vib.frq^4;% co-variance of the input (acceleration)   deriva
```

State equation parameters.

x: state; x = [P, V]': the position and velocity of the target. u: input; the acceleration of the target x(M+1) = F * x(M) + G * u(M)

```
F = [1, t_b; 0, 1]; % time-invariant state transition model
G = [0; t_b];       % time-invariant control input model
H = zeros(1,2);     % time-variant observation model

K = zeros(2,1,N);   % Kalman gain

% Start the Kalman filter recursion; n = i-1;
for i = 11:1:N-1
    % Linearization of the observation function.
    % NOTE: The observation function depends on the observations!
```

```
    % Therefore, the Kalman Gain, the state estimates, and the estimate of
    % the covariance of the state error are also functions of the
    % observations.

%     % complex-value case
%     % no averaging of prediction points
%       MPX(:,1,i+1) = (PX(:,1,i+1));
%     % average two concevative points
%       MPX(:,1,i+1) = (PX(:,1,i+1)+PX(:,1,i))/2;
%     % average 5 consecutive points
%       MPX(:,:,i+1) = (PX(:,:,i+1)+PX(:,:,i)+PX(:,:,i-1)+PX(:,:,i-2)+...
%                         PX(:,:,i-3))/5;
%     % average 6 consecutive points
%     MPX(:,:,i+1) = (PX(:,:,i+1)+PX(:,:,i)+PX(:,:,i-1)+PX(:,:,i-2)+ ...
%         PX(:,:,i-3)+PX(:,:,i-4))/6;
%         % average 7 consecutive points
%         MPX(:,:,i+1) = (PX(:,:,i+1)+PX(:,:,i)+PX(:,:,i-1)+PX(:,:,i-2)+...
%                         PX(:,:,i-3)+PX(:,:,i-4)+PX(:,:,i-5))/7;
      % average eleven consecutive points
      MPX(:,:,i+1) = (PX(:,:,i+1)+PX(:,:,i)+PX(:,:,i-1)+PX(:,:,i-2)+...
                    PX(:,:,i-3) +PX(:,:,i-4)+PX(:,:,i-5)+ ...
                    PX(:,:,i-6)+PX(:,:,i-7)+PX(:,:,i-8))/10;
%      % average 20 consecutive points
%      MPX(:,:,i+1) = (PX(:,:,i+1)+PX(:,:,i)+PX(:,:,i-1)+PX(:,:,i-2)+ ...
%         PX(:,:,i-3)+PX(:,:,i-4)+PX(:,:,i-5)+PX(:,:,i-6)+PX(:,:,i-7) ...
%         + PX(:,:,i-8)+PX(:,:,i-9)+ PX(:,:,i-10)+PX(:,:,i-11)...
%         + PX(:,:,i-12)+PX(:,:,i-13)+ PX(:,:,i-14)+PX(:,:,i-15) ...
%         + PX(:,:,i-16)+PX(:,:,i-17)+ PX(:,:,i-18))/20;
```

```
tmp_exp = exp(-1j * PI2_lambda * (2 * MPX(1,1,i+1) + t_b * ...
          MPX(2,1,i+1)) - 1j * pi /2);

H(1,1) = 4 * PI2_lambda * tgt_ref(i+1) * sin(PI2_lambda * t_b * ...
         MPX(2,1,i+1)) * tmp_exp * exp(-1j*pi/2);
H(1,2) = 2 * PI2_lambda * t_b * tgt_ref(i+1) * cos(PI2_lambda * ...
    t_b * MPX(2,1,i+1)) * tmp_exp -  2* PI2_lambda * t_b * ...
    tgt_ref(i+1) * sin(PI2_lambda * t_b * MPX(2,1,i+1)) * ...
    tmp_exp * exp(-1j*pi/2);

% real part case
%     tmp_phs = -PI2_lambda * (2 * PX(1,1,i+1) + t_b * PX(2,1,i+1)) ...
%               - pi / 2;
%     H(1,1) = 2 * tgt.sigma * PI4_lambda * sin(PI2_lambda * t_b * ...
%              PX(2,1,i+1)) * sin(tmp_phs + tgt_phs_ref(i+1));
%     H(1,2) = 2 * tgt.sigma * PI2_lambda * t_b * cos(PI2_lambda * ...
%              t_b * PX(2,1,i+1)) * cos(tmp_phs+ tgt_phs_ref(i+1)) ...
%              + 2 * tgt.sigma * PI2_lambda * t_b * sin(PI2_lambda *...
%              t_b * PX(2,1,i+1)) * sin(tmp_phs+ tgt_phs_ref(i+1));

% Kalman Gain
K(:,:,i+1) = (CPX(:,:,i+1) * H') / (H * CPX(:,:,i+1) * H' + var_w);

% Updated State
EX(:,:,i+1) = PX(:,:,i+1) + K(:,:,i+1) * (Y(i+1) - H * PX(:,:,i+1));

% Predicted State
```

```
    PX(:,:,i+1+1) = F * EX(:,:,i+1);

    % Updated Covariance of System Error
    CEX(:,:,i+1) = CPX(:,:,i+1) - K(:,:,i+1) * H * CPX(:,:,i+1);

    % Predicted Covariance of System Error
    CPX(:,:,i+1+1) = F * CEX(:,:,i+1) * F' + G * var_u * G';

end;
```

Estimated Velocity

```
est_v = reshape(real(EX(2,1,:)),N,1);% estimated target velocity
est_v = est_v-mean(est_v);           % estimated target velocity w/out bias
est_spc_ekf = abs(fft(est_v));       % periodicity of target velocities

% Plot estimated velocity
figure(110)

subplot(2,1,1);
plot(est_v); %??
hold on;
plot(vib_vlc,'k-.');
xlabel('slow time');
ylabel('Velocity (mm/s)');
title({'Estimated velocity of a 1 mm, 8 Hz vibrating target', ...
       'using the EKF with SNR = 11 dB',...
       '10 term avg. for noise suppression'});
```

```
legend('Est. Target Velocity', 'True Target Velocity')

subplot(2,1,2);
plot((1:spc_upper-1)/N*prf, est_spc_ekf(1:spc_upper-1));
xlabel('Frequency (Hz)');
ylabel('Magnitude (AU)');
title('Target''s Estimated Vibrating Frequency')

% Target's vibration frequency estimation from velocity estimates
zulu1 = est_spc_ekf(1:spc_upper)';
[alpha1,bravo1] = max(zulu1);
charlie = (0:spc_upper)/N*prf;
est_v1 = charlie(bravo1);
zulu1(:,bravo1) = 0;
[alpha2,bravo2] = max(zulu1);
est_v2 = charlie(bravo2);
if abs(bravo1-bravo2) < 4
   tot_est_v = (est_v1 + est_v2)/2;
else
    if alpha1>alpha2
        tot_est_v = charlie(bravo1);
    else
        tot_est_v = charlie(bravo2);
    end
end
disp('Target''s estimated vibration frequency from velocity estiamtes: ')
disp(tot_est_v)
```

```
Target's estimated vibration frequency from velocity estiamtes:
    8.0296
```

Plot estimated position

```
est_p = reshape(real(EX(1,1,:)),N,1);   % etimated target position
est_p = est_p - mean(est_p);            % etimated target pos. w/out bias
est_spc2_ekf = abs(fft(est_p));         % periodicity of target position

figure(120)
subplot(2,1,1);
plot(est_p,'r');
hold on;
plot(vib_dis,'k-.');
xlabel('slow time');
ylabel('Displacement (m)');
title({'Estimated position'}) %with SNR = 11 dB',...
%        '20 term avg. for noise suppression'});
legend('Est. Target Position', 'True Target Position')
axis([0 N -.005 .005])
subplot(2,1,2);
plot((0:spc_upper-1)/N*prf, est_spc2_ekf(1:spc_upper),'r');
xlabel('Frequency (Hz)');
ylabel('Magnitude (AU)');
title('Target''s Estimated Vibrating Frequency')
```

Target's vibration frequency estimation from position estiamtes

```
zulu2 = est_spc2_ekf(1:spc_upper)';
[alpha3,bravo3] = max(zulu2);
charlie2 = (0:spc_upper)/N*prf;
est_p1 = charlie2(bravo3);
zulu2(:,bravo3) = 0;
[alpha4,bravo4] = max(zulu2);
est_p2 = charlie2(bravo4);
if abs(bravo3-bravo4) < 4
   tot_est_p = (est_p1 + est_p2)/2;
else
    if alpha3>alpha4
        tot_est_p = charlie2(bravo3);
    else
        tot_est_p = charlie2(bravo4);
    end
end
disp('Target''s estimated vibration frequency from postion estiamtes: ')
disp(tot_est_p)

Target's estimated vibration frequency from postion estiamtes:
    8.0296



tot_est_frq = (tot_est_v + tot_est_p)/2;
disp('Target''s estimated vibration frequency averaging the velocity and ')
disp('postion estimates: ')
disp(tot_est_frq)
```

```
Target's estimated vibration frequency averaging the velocity and
postion estimates:
    8.0296
```

Extended Kalman Filter for Multicomponent Vibrations

Contents

Extended Kalman Filter for DPCA-SAR

```
% Multi-component sinusoidal vibration
% increasing linear chirp

% Qi Wang; July 11, 2012
% Justin Campbell; May 25, 2016
```

Begin Program

```
clc;
clear;
close all;
```

Initializing Parameters

```
fc = 1.6e10;            % Center frequency
c = 3e8;                % Propagation Velocity
lambda_c = c / fc;      % Wavelength
V = 175;                % Platform Velocity (meters)
Rc = 10000;             % Range to image center (meters)
N = 1000;               % Number of samples
rhoy = 0.33;            % Azimuth res
diameter.y = rhoy * N;  % Azimuth physical size
ka = 1.58;              % Armin reference (effective prf paper)
%ka = 2;
prf = V*ka*diameter.y/(lambda_c*Rc);    % Pulse Repetition Frequency
ts = 1 / prf;           % PRI (pulse repetition interval)

% Frequently used constants
PI2 = pi * 2;
PI4 = pi * 4;

PI2_lambda = PI2 / lambda_c;
PI4_lambda = PI4 / lambda_c;
```

```
ky = (PI4*fc*V)/(c*Rc*prf); % scaling parameter
```

Target Information

```
tgt.sigma = 1e-4;       % Reflectance magnitude
tgt.y = 3;              % Azmmith Position
tgt.phi = 0.1 * pi;     % Initial phase

% Total Reflectance
tgt_phs_ref = -ky * tgt.y * (1:N) + tgt.phi;
tgt_ref = tgt.sigma * exp(1j * tgt_phs_ref);
```

Target's Vibration information

```
vib.amp1 = 1e-3;    % 1 mm vibration amplitude
vib.frq1 = 5;       % vibration frequency 5 Hz
vib.phi1 = 0;       % zero initial vibration displacement
vib.amp2 = .75e-3;  % .75 mm vibration amplitude
vib.frq2 = 12;      % vibration frequency 12 Hz
vib.phi2 = pi/2;    % zero initial vibration displacement (opposite amp)

M_b = 10;                   % determined by the baseline, V and prf
t_b = M_b * ts;             % time delay between two antennas
st = (1:N) * ts + t_b;      % timing of pulses

vib_dis = vib.amp1 * sin(PI2 * vib.frq1 * (st) + vib.phi1) + vib.amp2 * ...
    sin(PI2 * vib.frq2 * (st) + vib.phi2);
vib_vlc = vib.amp1 * PI2 * vib.frq1 * sin(PI2 * vib.frq1 * (st) + ...
```

```
    vib.phi1) + vib.amp2 * PI2 * vib.frq2 * sin(PI2 * vib.frq2 * ...
    (st) + vib.phi2);
```

Simulating the observations

```
soi_dualbeam = zeros(N,1);
for i = 1:N
    tau = i * ts;
    dis2 = vib.amp1 * sin(PI2 * vib.frq1 * (tau+t_b) + vib.phi1) + ...
        vib.amp2 * sin(PI2 * vib.frq2 * (tau+t_b) + vib.phi2);
    dis1 = vib.amp1 * sin(PI2 * vib.frq1 * (tau) + vib.phi1) + ...
        vib.amp2 * sin(PI2 * vib.frq2 * (tau) + vib.phi2);
    soi_dualbeam(i) = tgt_ref(i) * (exp(-1j* PI4_lambda * dis2) - ...
        exp(-1j* PI4_lambda * dis1));
end

soi_dualbeam_pure = soi_dualbeam;

snr = 15;
var_w = tgt.sigma^2 / 10^(snr/10);
w = sqrt(var_w/2) * randn(N,1) + 1j * sqrt(var_w/2) * randn(N,1);
soi_dualbeam = soi_dualbeam + w;

figure(1)
subplot(2,1,1)
plot(abs(soi_dualbeam));
xlabel('Time (s)');
ylabel('Magnitude (AU)');
```

```
title({'Est. a multiple-component vibration'});
subplot(2,1,2)
est_spc_mag = abs(fft(abs(soi_dualbeam)-mean(abs(soi_dualbeam))));
spc_upper = 200;
plot((0:spc_upper-1)/N*prf, est_spc_mag(1:spc_upper));
xlabel('Frequency (Hz)');
ylabel('Magnitude (AU)');
```

Start the Kalman Filtering

```
X = zeros(2,1,N+1);     % State of the vibrating target [ pos., vel. ]
Y = soi_dualbeam;       % Observation (range compressed slow time signal)

EX = zeros(2,1,N);      % State estimate (correction)
PX = zeros(2,1,N+5);    % State prediction
MPX = zeros(2,1,N+1);   % State prediction average over several pulses

CEX = zeros(2,2,N);                % system error covariance (correction)
CPX = zeros(2,2,N+1);              % system error covariance (prediction)

% Initial conditions
%X(:,:,1) = [0;vib.amp*vib.frq*PI2]; % the initial target state ...
X(:,:,1) = [0;0];                  % the initial target state ...
PX(:,:,1) = X(:,:,1);
```

In these simulations we assume the prf is significantly faster than the

target's vibration fequency. Therefore, the target's state (position, velocity) will re-

mained relatively unchanged between several successive pulses. Therefore, I intialize the first couple of terms with the same values.

Position is kinda orthogonal to velocity. Recall target displacement is 1 mm cvp = 1e-6/2; cvv = cvp * PI2^2 * 30^2; CPX(:,:,1) = [cvp, 0; 0, cvv]; % co-cvariance of the intial vib. pos. var_u = cvv * PI2^4 * 30^4;

```
cvp = (vib.amp1+vib.amp2)^2;
cvv = cvp * PI2^2 * (vib.frq1^2 + vib.frq2^2);
CPX(:,:,1) = [cvp, 0; 0, cvv]; % co-cvariance of the intial vib. pos.
var_u = cvp * PI2^4 *(vib.frq1^2 + vib.frq2^2);
```

State equation parameters.

x: state; x = [P, V]': the position and velocity of the target. u: input; the acceleration of the target x(M+1) = F * x(M) + G * u(M)

```
F = [1, t_b; 0, 1]; % time-invariant state transition model
G = [0; t_b];       % time-invariant control input model
H = zeros(1,2);     % time-variant observation model

K = zeros(2,1,N);   % Kalman gain

% Start the Kalman filter recursion; n = i-1;
for i = 11:1:N-1
    % Linearization of the observation function.
    % NOTE: The observation function depends on the observations!
    % Therefore, the Kalman Gain, the state estimates, and the estimate of
```

```
    % the covariance of the state error are also functions of the
    % observations.

    % complex-value case
        % no averaging of prediction points
%        MPX(:,1,i+1) = (PX(:,1,i+1));
%         % average two concevative points
%         MPX(:,1,i+1) = (PX(:,1,i+1)+PX(:,1,i))/2;
%         % average 5 consecutive points
%         MPX(:,:,i+1) = (PX(:,:,i+1)+PX(:,:,i)+PX(:,:,i-1)+PX(:,:,i-2)+...
%                         PX(:,:,i-3))/5;
%     % average 6 consecutive points
%     MPX(:,:,i+1) = (PX(:,:,i+1)+PX(:,:,i)+PX(:,:,i-1)+PX(:,:,i-2)+ ...
%         PX(:,:,i-3)+PX(:,:,i-4))/6;
        % average 7 consecutive points
        MPX(:,:,i+1) = (PX(:,:,i+1)+PX(:,:,i)+PX(:,:,i-1)+PX(:,:,i-2)+...
                        PX(:,:,i-3)+PX(:,:,i-4)+PX(:,:,i-5))/7;
%      % average ten consecutive points
%      MPX(:,:,i+1) = (PX(:,:,i+1)+PX(:,:,i)+PX(:,:,i-1)+PX(:,:,i-2)+...
%                      PX(:,:,i-3) +PX(:,:,i-4)+PX(:,:,i-5)+ ...
%                      PX(:,:,i-6)+PX(:,:,i-7)+PX(:,:,i-8))/10;
%     % average 20 consecutive points
%     MPX(:,:,i+1) = (PX(:,:,i+1)+PX(:,:,i)+PX(:,:,i-1)+PX(:,:,i-2)+ ...
%         PX(:,:,i-3)+PX(:,:,i-4)+PX(:,:,i-5)+PX(:,:,i-6)+PX(:,:,i-7) ...
%         + PX(:,:,i-8)+PX(:,:,i-9)+ PX(:,:,i-10)+PX(:,:,i-11)...
%         + PX(:,:,i-12)+PX(:,:,i-13)+ PX(:,:,i-14)+PX(:,:,i-15) ...
%         + PX(:,:,i-16)+PX(:,:,i-17)+ PX(:,:,i-18))/20;
```

```
%     tmp_exp = exp(-1j * (-ky*tgt.y*i*ts + vib.phi - PI2_lambda* ...
%              (2*MPX(1,1,i+1) + t_b * MPX(2,1,i+1)) -  pi/2));

tmp_exp = exp(-1j * PI2_lambda * (2 * MPX(1,1,i+1) + t_b * ...
          MPX(2,1,i+1)) - 1j * pi /2);

H(1,1) = 4 * PI2_lambda * tgt_ref(i+1) * sin(PI2_lambda * t_b * ...
         MPX(2,1,i+1)) * tmp_exp * exp(-1j*pi/2);
H(1,2) = 2 * PI2_lambda * t_b * tgt_ref(i+1) * cos(PI2_lambda * ...
    t_b * MPX(2,1,i+1)) * tmp_exp -  2* PI2_lambda * t_b * ...
    tgt_ref(i+1) * sin(PI2_lambda * t_b * MPX(2,1,i+1)) * ...
    tmp_exp * exp(-1j*pi/2);

% Kalman Gain
K(:,:,i+1) = (CPX(:,:,i+1) * H') / (H * CPX(:,:,i+1) * H' + var_w);

% Updated State
EX(:,:,i+1) = PX(:,:,i+1) + K(:,:,i+1) * (Y(i+1) - H * PX(:,:,i+1));

% Predicted State
PX(:,:,i+1+1) = F * EX(:,:,i+1);

% Updated Covariance of System Error
CEX(:,:,i+1) = CPX(:,:,i+1) - K(:,:,i+1) * H * CPX(:,:,i+1);

% Predicted Covariance of System Error
CPX(:,:,i+1+1) = F * CEX(:,:,i+1) * F' + G * var_u * G';
```

```
end;

est_v = reshape(real(EX(2,1,:)),N,1);
est_v = est_v - mean(est_v);
est_spc_ekf = abs(fft(est_v));
figure(11)
subplot(2,1,1);
plot(est_v);
hold on;
plot(vib_vlc,'k-.');
xlabel('Time (s)');
ylabel('Velocity (m/s)');
title({'Estimated velocity of a multiple-component vibration' ...
 '(1 mm, 5 Hz and 0.5 mm, 12 Hz)\newline using the EKF with SNR = 15 dB'});
subplot(2,1,2);

plot((0:spc_upper-1)/N*prf, est_spc_ekf(1:spc_upper));
xlabel('Frequency (Hz)');
ylabel('Magnitude (AU)');

est_p = reshape(real(EX(1,1,:)),N,1);
est_p = est_p - mean(est_p);
est_spc2_ekf = abs(fft(est_p));
figure(12)
subplot(2,1,1);
plot(est_p);
hold on;
plot(vib_dis,'k-.');
```

```
xlabel('Time (s)');
ylabel('Displacement (m)');
title({'Estimated Position' ...
      'multiple-component vibration'});
legend('Est. Target Position','True Target Position')
subplot(2,1,2);

plot((0:spc_upper-1)/N*prf, est_spc2_ekf(1:spc_upper));
xlabel('Frequency (Hz)');
ylabel('Magnitude (AU)');
title('Target''s Estimated Vibrating Frequency')


zulu2 = est_spc2_ekf(1:spc_upper)';
[alpha3,bravo3] = max(zulu2);
charlie2 = (0:spc_upper)/N*prf;
est_p1 = charlie2(bravo3);
zulu2(:,bravo3) = 0;
[alpha4,bravo4] = max(zulu2);
est_p2 = charlie2(bravo4);
% if abs(bravo3-bravo4) < 4
%    tot_est_p = (est_p1 + est_p2)/2;
% else
%     if alpha3>alpha4
%         tot_est_p = charlie2(bravo3);
%     else
%         tot_est_p = charlie2(bravo4);
%     end
% end
```

```
disp('Target''s estimated vibration frequency from postion estiamtes: ')
disp(est_p1)
disp('and')
disp(est_p2)

Target's estimated vibration frequency from postion estiamtes:
    4.8664

and
   12.1660
```

References

[1] Xueru Bai, Mengdao Xing, Feng Zhou, Guangyue Lu, and Zheng Bao. Imaging of micromotion targets with rotating parts based on empirical-mode decomposition. *Geoscience and Remote Sensing, IEEE Transactions on*, 46(11):3514–3523, 2008.

[2] Victor C Chen, Fayin Li, Shen-Shyang Ho, and Harry Wechsler. Micro-doppler effect in radar: phenomenon, model, and simulation study. *Aerospace and Electronic Systems, IEEE Transactions on*, 42(1):2–21, 2006.

[3] Gordon Chin, Scott Brylow, Marc Foote, James Garvin, Justin Kasper, John Keller, Maxim Litvak, Igor Mitrofanov, David Paige, Keith Raney, et al. Lunar reconnaissance orbiter overview: The instrument suite and mission. *Space Science Reviews*, 129(4):391–419, 2007.

[4] Shen Chiu. Performance of radarsat2 sar-gmti processors at high sar resolutions. Technical report, DTIC Document, 2000.

[5] Shen Chiu and Chuck Livingstone. A comparison of displaced phase centre antenna and along-track interferometry techniques for radarsat-2 ground moving target indication. *Canadian Journal of Remote Sensing*, 31(1):37–51, 2005.

[6] Ian G Cumming and Frank Hay-chee Wong. *Digital processing of synthetic aperture radar data: algorithms and implementation*. Artech house, 2005.

[7] Armin W Doerry. Performance limits for synthetic aperture radar. Technical report, DTIC Document, 2006.

[8] Armin W Doerry and Fred M Dickey. Synthetic aperture radar. *Optics and photonics news*, 15(11):28–33, 2004.

[9] R Fitzgerald. Divergence of the kalman filter. *IEEE Transactions on Automatic Control*, 16(6):736–747, 1971.

[10] Charles VJ Jakowatz, Daniel E Wahl, Paul H Eichel, Dennis C Ghiglia, and Paul A Thompson. *Spotlight-Mode Synthetic Aperture Radar: A Signal Processing Approach: A Signal Processing Approach*. Springer Science & Business Media, 2012.

[11] Simon J Julier and Jeffrey K Uhlmann. Unscented filtering and nonlinear estimation. *Proceedings of the IEEE*, 92(3):401–422, 2004.

[12] Rudolph Emil Kalman. A new approach to linear filtering and prediction problems. *Journal of basic Engineering*, 82(1):35–45, 1960.

[13] Xiang Li, Bin Deng, Yuliang Qin, Hongqiang Wang, and Yanpeng Li. The influence of target micromotion on sar and gmti. *Geoscience and Remote Sensing, IEEE Transactions on*, 49(7):2738–2751, 2011.

[14] H Vincent Poor. *An introduction to signal detection and estimation*. Springer Science & Business Media, 2013.

[15] R Keith Raney. Synthetic aperture imaging radar and moving targets. *Aerospace and Electronic Systems, IEEE Transactions on*, (3):499–505, 1971.

[16] Maurice Ruegg, Erich Meier, and Daniel Nuesch. Constant motion, acceleration, vibration, and rotation of objects in sar data. In *Remote Sensing*, pages 598005–598005. International Society for Optics and Photonics, 2005.

[17] Maurice Rüegg, Erich Meier, and Daniel Nüesch. Vibration and rotation in millimeter-wave sar. *Geoscience and Remote Sensing, IEEE Transactions on*, 45(2):293–304, 2007.

[18] Mehrdad Soumekh. *Synthetic aperture radar signal processing*. New York: Wiley, 1999.

[19] T Sparr and B Krane. Micro-doppler analysis of vibrating targets in sar. In *Radar, Sonar and Navigation, IEE Proceedings-*, volume 150, pages 277–83. IET, 2003.

[20] Robert F Stengel. *Optimal control and estimation*. Courier Corporation, 2012.

[21] Stanley I Tsunoda, Frank Pace, Jesse Stence, Marv Woodring, William H Hensley, Armin W Doerry, and Bruce C Walker. Lynx: A high-resolution synthetic aperture radar. In *AeroSense'99*, pages 20–27. International Society for Optics and Photonics, 1999.

[22] Juan G Vargas-Rubio and Balu Santhanam. An improved spectrogram using the multiangle centered discrete fractional fourier transform. In *Acoustics, Speech, and Signal Processing, 2005. Proceedings.(ICASSP'05). IEEE International Conference on*, volume 4, pages iv–505. IEEE, 2005.

[23] Eric Wan. Sigma-point filters: An overview with applications to integrated navigation and vision assisted control. In *Nonlinear Statistical Signal Processing Workshop, 2006 IEEE*, pages 201–202. IEEE, 2006.

[24] Qi Wang. Time-frequency methods for vibration estimation using synthetic aperture radar. 2013.

[25] Qi Wang, Majeed M Hayat, Balu Santhanam, and Tom Atwood. Sar vibrometry using fractional fourier transform processing. In *SPIE Defense, Security, and Sensing*, pages 73080B–73080B. International Society for Optics and Photonics, 2009.

[26] Qi Wang, Matthew Pepin, Ryan J Beach, Ralf Dunkel, Tom Atood, Armin W Doerry, Balu Santhanam, Walter Gerstle, and Majeed M Hayat. Demonstration of target vibration estimation in synthetic aperture radar imagery. In *Geoscience and Remote Sensing Symposium (IGARSS), 2011 IEEE International*, pages 4083–4086. IEEE, 2011.

[27] Qi Wang, Matthew Pepin, Ryan J Beach, Ralf Dunkel, Tom Atwood, Balu Santhanam, Walter Gerstle, Armin W Doerry, and Majeed M Hayat. Sar-based vibration estimation using the discrete fractional fourier transform. *Geoscience and Remote Sensing, IEEE Transactions on*, 50(10):4145–4156, 2012.

[28] Qi Wang, Matthew Pepin, Balu Santhanam, Tom Atwood, and Majeed M Hayat. Sar-based vibration retrieval using the fractional fourier transform in slow time. In *SPIE Defense, Security, and Sensing*, pages 766911–766911. International Society for Optics and Photonics, 2010.

[29] Qi Wang, Balu Santhanam, Matthew Pepin, and Majeed M Hayat. Performance analysis on synthetic aperture radar-based vibration estimation in clutter. In *Signals, Systems and Computers (ASILOMAR), 2012 Conference Record of the Forty Sixth Asilomar Conference on*, pages 217–221. IEEE, 2012.

[30] Qi Wang, Mengdao Xing, Guangyue Lu, and Zheng Bao. High-resolution three-dimensional radar imaging for rapidly spinning targets. *Geoscience and Remote Sensing, IEEE Transactions on*, 46(1):22–30, 2008.

[31] Yuhong Zhang. Along track interferometry synthetic aperture radar (ati-sar) techniques for ground moving target detection. Technical report, DTIC Document, 2006.